Provision of Controlled and Consistent Light Distribution Over an Uneven Topography to Maximize Efficacy of Machine-Vision based Defect Identification

Mark Gerges

A thesis

submitted in partial fulfillment of the

requirements for the degree of

Master of Science in Engineering

University of Washington

2021

Committee:

Xu Chen

Santosh Devasia

Jaehyun Chung

Program Authorized to Offer Degree:

Mechanical Engineering

University of Washington

Abstract

Provision of Controlled and Consistent Light Distribution Over an Uneven Topography to Maximize Efficacy of Machine-Vision based Defect Identification

Mark Gerges

Chair of the Supervisory Committee:
Xu Chen, Assistant Professor
Mechanical Engineering

Current manual inspection has risen as a bottleneck in aircraft component manufacture. Not only are conventional inspections slow and tiring, but the outcomes are also subjective and prone to inaccuracies, leading to limited streamlining of production, and in turn, a negative impact on competitive pricing. As a result, robotization and automation have become essential and have made significant strides in recent gas turbine production. At the root of the problem, challenges manufacturers face include the large variety of materials, variety of shapes and topographies, and automation systems' reliability. Automating the visual inspection process requires the employment of an optomechanical system. Such a system must capture images of a work-piece and then analyze the resulting pixel-domain data. Under properly controlled illumination, the captured images would be handled by the machine vision system easily and with a high degree of

reliability and repeatability than manual inspection. This work provides controlled and consistent lighting methodologies to facilitate quality image data collection over complex-shaped, highly reflective surfaces. Two quantities were controlled: the luminous intensity of the light source and the illuminance of the surface under consideration. The central approach entails using arrays of independently controlled light sources to generate different lighting patterns, structures, and colors. Such results consider the geometry and 3D pose of parts in the environment and the surface topography of the work-piece to be inspected, hence amplifying a classical image capturing system (patent application serial no. 63/180,631). We discuss the mathematical problem formulation, the analytic solution, the optimality of the proposed shape-adaptive lighting, and experimental results in the imaging of curved parts common in aerospace manufacturing.

Furthermore, we provide four solution configurations and compare the resulting defect identification using a transfer-learning deep neural network. The results assisted in creating an identification accuracy of more than 95 percent using only sparse data. In particular, compared with a non-shape-adaptive configuration, the proposed methods increased training and validation accuracy by 1.8 % and 1.6 %, respectively, and reduced false alarms and miss rates by 1.0 % and 2.25 %.

TABLE OF CONTENTS

LIST OF FIGURES

LIST OF TABLES

ACKNOWLEDGEMENTS

This paper and the research behind it would not have been possible without the exceptional support of my advisor, Professor Xu Chen. His enthusiasm, knowledge, and exacting attention to detail have been an inspiration and kept my work on track from my first encounter with the physics of light to the final draft of this paper.

And of course, a special thank you to the courteous committee members, Professor Santosh Devasia and Professor Jaehyun Chung, who honored me with their attendance and inquisitive and educational queries into the insights and adaptability of the system.

Further, I express my gratitude to The members of the University of Washington MACS lab at MEB who contributed to image capture, motion, and mapping of the project; Dan Wang, Hui Xiao, Abhishek Kulkarni, and Michael Gagnier. I also Thank our colleagues at the University of Connecticut, Dr. Jiong Tang, Dr. Shalabh Gupta, Qianyu Zhou, Jing Yang, and Christian Schirmer, who worked on the project's machine learning aspect. Their critical feedback in the iterative improvements to the system was insurmountably valuable. And of course my gratitude also goes to the Representatives of GKN Aerospace: Alexander Strzelecki, Andreas Andersson, and Martin Philo who helped the project come true.

Last but not least, I am also grateful for the unwavering support of my family, consisting of my Grandmother Violette, Father Hani, Mother Heba, siblings Mina, Carol, and Violette, and of course, my niece Angela.

Chapter 1. INTRODUCTION

Manual/visual inspection is the process that human operators and quality inspectors follow to inspect units during production or assembly visually. Inspectors rely on the naked eye, a microscope, or a specialized instrument to review particular areas for quality. Figure 1 shows the process in action where the first illustration is the inspection of a circuit board and its components, and the second is an on-site weld inspection.

Figure 1: Visual Inspection (1) Circuit Board [1] (2) On-site Weld [2]

The main benefit of manual inspection is that inspectors require a less technical background to detect defects. However, the drawbacks are related to the varying accuracy of human inspectors subject to factors such as fatigue, turnover, and inconsistent classification of defects, leading to quality variations across operator shifts, and hence the cost of reduced throughput. Another drawback would be that only known issues outlined in operating procedures are inspected; unanticipated defects are typically not discovered by inspectors. Furthermore, in many cases, a data record of the inspections is not kept. The typical manual inspection process lacks modern traceability [3]. The level of data logging does vary depending on the criticality of the work, specifically in welds in the oil and gas industry where I have my work experience, where each

spool's, joints, welds, and hydro tests are tracked and recorded; however, in residential infrastructure, such records may not be readily available.

To circumvent the shortcomings of manual inspection, optomechanical systems that incorporate computer vision are aggressively pursued by industries, more commonly known as machine vision. This is a term that covers the technologies and methods used to provide imaging-based automatic inspection and analysis. These systems use a camera to view an image, a computer vision algorithm then processes and interprets said image, and finally, an instruction is given to other components in the system to act upon that data. A comparison between both manual and machine vision-based inspections is illustrated as the camera representing the eyes, the Conveyor/Robotic arm for part transportation/manipulation representing the hands, and finally, the Computer Vision package for the analysis, processing, and pattern matching of images, representing the brain. The benefits of machine vision systems are embodied in their accurate detection of defects due to the increased consistency and reliability since human error and fatigue are eliminated, which in turn eliminates throughput variations. Another would be the system's high customizability. Each implementation is typically optimized for one particular defect/component; and, increased robustness is achievable through more training. Finally, Due to the automation of the system, traceability and document control are easily implemented in the computer vision package. However, like manual inspection, machine vision only detects known defects that have been programmed into the system, which also means, they are not flexible to automatically incorporate changes to the inspected parts, surface finishes, and lighting conditions. Hence requiring that every change is programmed and trained into the system [3]. The increases in accuracy, reliability, and traceability, and the reduction of cost to throughput, justifies the application of machine vision on production and assembly lines, as changes in the

environmental, spatial, and geometric conditions are reduced on these lines as a result of mass production making them predictable and simpler to control. A diverse range of industries has benefited from recent advances in machine vision technologies: e.g., in the general manufacturing industry, robotic guidance, part identification, visual inspection, process control, characterization, fault detection, and inventory management [4, 5, 6, 7, 8, 9]. Moreover, other industry-specific applications such as aerospace with aerial refueling [10], agricultural produce and forestry in disease and contamination identification, and leaf recognition [11, 12, 13] have also benefited from said breakthroughs.

Extending this discussion into the aerospace manufacturing industry, which is the focus of this work, shows that current manual inspection has risen as a bottleneck in aircraft component manufacture. In the $68 billion gas turbine engine market (in 2017, projected to rise to $92B in 2022 [14]), for example, defects as minor as scratches and pits could lead to imbalances in airflow and part fatigue which results in premature engine wear and even engine failures [15, 16, 17]. Not only are conventional inspections slow and tiring, but the outcomes are also subjective and prone to inaccuracies, leading to limited streamlining of production, in turn, a negative impact on competitive pricing [18]. As a result, robotization and automation have become essential and have made significant strides in recent gas turbine production [19]. At the root of the problem, challenges that face manufacturers include the large variety of materials, variety of shapes and topographies, and automation systems' reliability. The variety of materials gives rise to different visual inspection requirements, as polymers and metals reflect light differently (regarding polarity, color, and reflectivity) and demand tailored inspection solutions [20].

On the other hand, different shapes and topographies cause more complex reflection patterns and more difficult imaging processes [21]. Due to the strict quality and accuracy standards, visual

and dimensional inspections remain labor-intensive and non-systematic, resulting in sub-optimal quantity and quality in production [22]. Automating the visual inspection process requires the employment of an optomechanical system. Such a system must capture images of a work-piece and then analyze the resulting pixel-domain data, rather than analyzing the physical work-piece itself. In both manual and machine vision-based inspections, there is a common denominator, which is the lighting. In this work, we aim to increase the adaptability of machine vision systems in this often-overlooked aspect. It is critical to understand how the light reflects off the surface desired to be studied to achieve this. The factors that affect the reflected lighting's integrity and characteristics are the work-piece material, its topography, and surface characteristics such as finish and color [20, 21, 23].

Furthermore, lighting can also affect how easy it is for the image capture system to produce an effective image. A good image is the result of proper focus and illumination of the desired surface. Images with poor contrast and uneven illumination require more compensation and computations from the image capture and analysis systems, ultimately increasing the processing time, the number of incorrect identifications, and analyses. Under properly controlled illumination, the captured images would be handled by the machine vision system easily and with a high degree of reliability and repeatability [20, 21, 24]. This thesis proposes a novel adaptive illuminance distribution for quality visual imaging and robotic inspections (patent application serial no. 63/180,631). The approach entails using multiple light sources tightly packed and equidistantly placed, with each being independently controllable. This hardware configuration allows for the generation of different lighting patterns, structures, and colors. From there, a constrained least-squares problem is formulated. This approach integrates (1) the geometry and 3D pose of work-pieces within the environment and (2) their surface topography.

In particular, we propose and physically implement five solutions of adaptive lighting and collected imaging data sets for a group of curved parts common in gas turbine manufacturing. And finally, the efficacy of the resulting defect identification is compared using a transfer learning deep neural network. The results appeared essential in perfecting the neural network learning performance, as through using less than 1500 raw images, the proposed lighting yielded over 95% identification accuracy with less than 5% false alarm rate. In particular, at such a nearly saturated benchmark, the shape-adaptive lighting increased training (+1.8 %) and validation (+1.6 %) accuracies and reduced false alarms (-1.0 %) and miss rates (-2.25 %) while using approximately 70% of the training data with no adaptive lighting and 30% using the proposed solutions. Improvements resulting from this research can empower the rising machine vision field to increase quality control standards by eliminating glare and lighting gradients, emphasizing surface defects and deviations over non-uniform and uneven topographies.

The remainder of this work is organized into six chapters. Chapter 2, Lighting, goes through surface reflectivity, lighting structure, and physics. Chapter 3, Adaptive Luminous Intensity, covers the sensor selection and calibration, modeling and controlling the luminous intensity to compensate for disturbances. Chapter 4, Adaptive Illuminance Distribution, covers the novel approach discussed above through the proof of concept, uneven topography strategy, and the solution by boxed least-squares. Chapter 5, Results and Comparison. Chapter 6, provides an extension to the optimal lighting solution by studying the effect of scaling the number of light sources and the angles of attack. Finally, Chapter 7 summarizes conclusions and consequent future improvements.

Chapter 2. LIGHTING

2.1 SELECTION

2.1.1 *Surface Reflectivity*

First, we address the behavior of light with the surface finish, as reflectivity and part shape/geometry affect the response of the machine vision system. Flat surfaces are uniform and easily illuminated; curved, uneven surfaces challenge illumination with changing topography; prismatic surfaces have sharp edges and/or steep slopes that are difficult to illuminate due to shadows and glints [20, 24]. In addition to geometry, the surface finish and reflectivity of the parts must be considered during an inspection. Specular and highly polished surfaces cause light to be reflected at an angle equal to and opposite to the angle of incidence. Diffuse surfaces are rough and dull, causing the incident light to be scattered in many directions. Directional surfaces have fine and uniform grooves that reflect light in a preferred direction dependent on the angle of incidence [23, 25, 26]. All three types of surfaces are encountered in this work and are considered in selecting the light source and lighting structure in section 2.1.3.

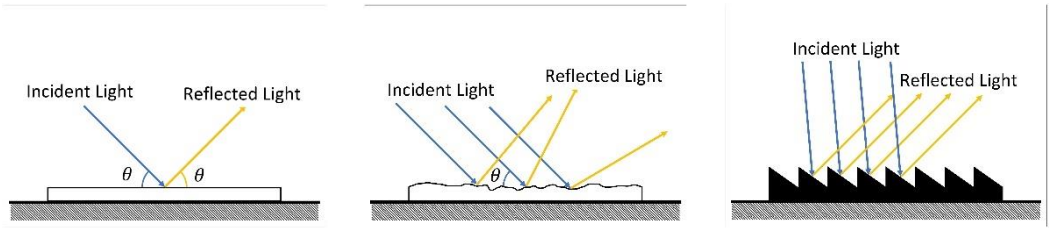

Figure 2: (1) Specular Surface (2) Diffuse Surface (3) Directional Surface

2.1.2 *Structure*

With the understanding of the different surface finishes and their behaviors, we direct our attention to the state-of-the-art lighting structures and shapes that are used in the field of machine vision. Interference and disturbances such as the sunlight and excessive room lighting

substantially impact the quality and consistency of inspection. One way to address the disturbances is to apply high-power strobing, which overwhelms the ambient contribution. Such an option, however, also has a high cost and challenging ergonomics. Besides, not all light sources (e.g., fluorescent lights) are capable of strobing. Another solution entails a physical enclosure that blocks environmental lighting and applies most suitably to small objects. In both cases, the lighting must be controlled to maintain a consistent luminosity [25, 26]. For the facilitation of the control, an enclosed work-space is created with the maximal possible sheltering from environmental disturbances. Furthermore, the structure, location, and pattern of lighting also affect the efficacy of the machine vision system. There are two parent structures/placements of light sources concerning the work-piece, source, and image capture system. The first is front illumination, where the light source and the receiver are on the same side, and the second being back illumination, where both are on opposite sides [25, 26]. Sections 2.1.2.1 and 2.1.2.2 discuss different types under the two-parent configurations and their benefits and drawbacks considered for the selection process in section 2.1.3.

2.1.2.1 Front Illumination

Here, direct or angled ring lights are characterized by having the image capture system at the light source center, leading to shadow-less illuminations. In addition, sharper angles of incidence on the surface lead to better detection of edges, scratches, and embossing.

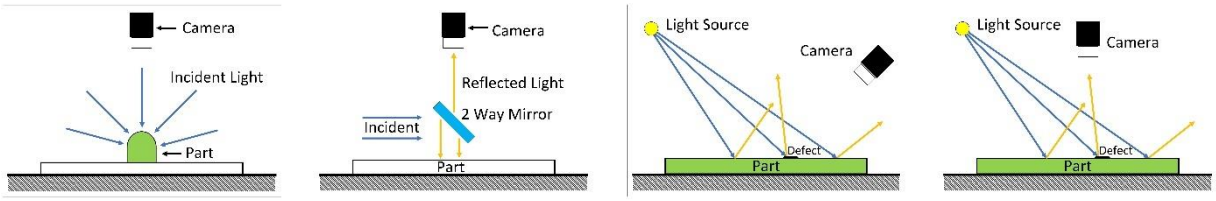

Figure 3: (1) Front (2) Co-Axial (3) Bright Field (4) Darkfield

Usually, this type of lighting is used for non-specular surfaces. Diffuse flat and coned ring lights are characterized by the even lighting distribution in the work-space; hence they are suitable for

inspecting specular surfaces with minimum glinting and shadows. Dome lights are characterized by the light sources reflecting off a dome-shaped concentrator and are used for curved and specular surfaces, as they minimize glinting and shadows. However, they require close proximity to the part, making it inapplicable to complex geometries (Figure 3 (1)). Co-axial lights are characterized by the 2-way mirror used to reflect light at an angle of 90^o onto the work-piece. These lights are used for specular surfaces and require very close proximity to the part (Figure 3 (2)). The last two types of front lighting considered for selection are dark and bright-field lighting. When the focused region is desired to be bright, and the inspected surfaces are uneven, dark-field lighting is most advisable (Figure 3 (4)), which results in the defects or nonconformities being darker. On the other hand, when the focus is on dark areas and flat surfaces are in question, bright-field lighting (Figure 3 (3)) is most advisable [25, 26].

2.1.2.2 Back Illumination

Two instances of this are shown in Figure 4. Dimensional analysis, gauging, hole inspection, and checking for the absence of components are the core benefits of back illumination [25, 26].

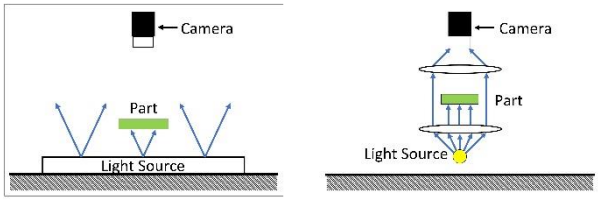

Figure 4: (1) Back-Light (2) Collimated Light

2.1.3 *Lighting shape/method Selection*

2.1.3.1 Shape

Considering both the surface finish behavior, we've established and the different lighting structures in the industry, we now start considering our specific application. Figure 5 shows examples of the different surface finishes we are analyzing. As evident, this work focuses on all three surface finishes and very curved and un-even topographies.

Figure 5: Surface finish and topography (1) Specular (2) Diffuse (3) Directional[1]

From sections 2.1.2.1 and 2.1.2.2, front and flat diffuse lighting rise as the most suitable for uneven topographies and different surface finishes. Also, diffuse dome/cylinder, dark- and bright-field lighting can help the targeted complex curved parts. For more general applicability of different lighting systems, readers are referred to [24]. Highlighting the surface finish and geometry relationship to lighting results in Figure 6, which provides the most suitable lighting type or types given the topography and surface finish of the inspected parts. As all surface finishes are encountered along with uneven and curved surface topographies, the bottom half of the diagram is considered (the approximate region the work considers is highlighted in red), resulting in flat diffuse and dome lighting standing out as the most suitable. As indicated earlier, the benefits of these lights are their reduction of glinting/glare and shadows, and hence, moving forward, these are the structures of lighting that we used.

[1] Data has been intentionally pixelated and distorted

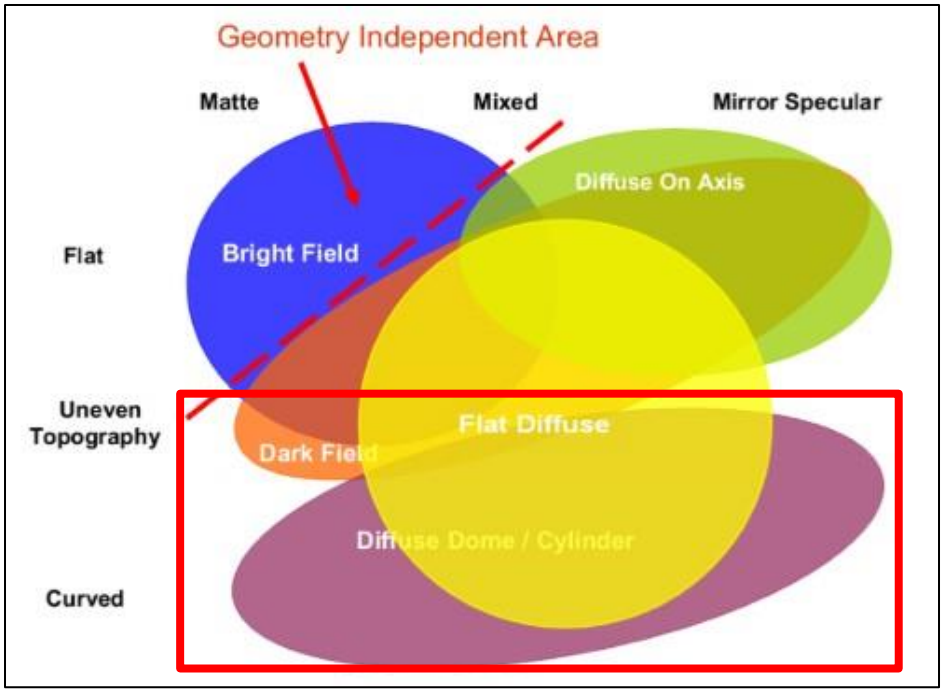

Figure 6: Surface finish and Geometry lighting selection [24]

2.1.3.2 Source

After the pattern and the methodology of lighting comes the selection of the light sources. We created a comparison of several light sources, specifically fluorescent, halogen, LED, xenon, and metal halide. A study of the capabilities and limitations is as follows.

Fluorescent

Fluorescent lights produce diffuse lighting that is cool and white and provide a large illumination area at low prices. However, they suffer from inflexible fixed shapes, short lifetimes, significant temperature drift, rapid aging, and long switching transients. Also, if Pulse Width Modulation (PWM) is used to control the brightness, a high frequency (22 kHz or more) ballast is required to reduce flicker interference [25, 26].

Halogen

Halogen lights provide high intensity and broad-spectrum lighting but suffer from a short lifetime and a significant drop off in brightness over the duty period. They also produce a large amount of heat, exhibit long switching transients, and require robust stabilization [25, 26].

LED

LEDs provide pulse and strobe capable monochromatic light. They have long lifetimes and small temperature drifts, and produce relatively low heat, and are stable, consistent, and cost-effective. However, in high-brightness applications, heat sinks are required, and if large-area lighting is needed, a diffuser should be used, which affects the integrity of illumination [25, 26].

Xenon

These lights provide a pulse and strobe capable monochromatic light capable of high-color temperatures (5,500 to 12,000 K). On the downside, they require high voltages, expensive electronics, and control. They also age faster than LEDs [25, 26].

Metal halide (Mercury/High-Pressure Sodium)

These are used in large-scale applications or when requiring very bright light sources. Still, they suffer from very high (e.g., 30 KV) working voltages, are expensive, and produce much heat [25, 26].

The Proposed Selection

Table 1 summarizes the relative strength of different lighting under a set of performance criteria relevant to the proposed robotic inspection. The criteria we focused upon were Output Stability, On-Time, Output Intensity, Reaction Time and Work Area/Distance. The LEDs showed to be most suitable for our requirements. It is deduced that the most suitable light sources for the application are LEDs in the supply of flat diffuse lighting. We implemented such a lighting

source in the work-space using a 120 LED shooting tent with a diffuser. This arrangement acts as the existing lights moving forward, and an additional set of auxiliary (compensatory) LED lights are employed and shall be covered in Chapter 4. In the next section, the mathematical problem is formulated, and through understanding the lighting physics, we create the proposed strategy for uneven topographies.

Table 1: Light Source Selection Process (Data source *1 – [25] *2 – [24])

Property (Out of 5)	**Wts.**	**LED**			**Halogen**			**Fluorescent**			**Xenon**		
		***1**	***2**	**Tot.**	***1**	***2**	**Tot.**	***1**	***2**	**Tot.**	***1**	***2**	**Tot.**
Life Exp.	0	5	5	5	2	1	1.5	3	3	3	3	4	3.5
App. Flexibility	0	4	5	4.5	3	3	3	2	2	2	2	3	2.5
Output Stability	**0.2**	**5**	**5**	**5**	**2**	**1**	**1.5**	**3**	**3**	**3**	**3**	**2**	**2.5**
Cost Eff./hr	0	4	4	4	2	3	2.5	3	4	3.5	2	3	2.5
Strobing	0	5		5	1		1	0		0	4		4
On time	**0.3**	**5**		**5**	**5**		**5**	**5**		**5**	**0**		**0**
Output Int.	**0.25**	**4**	**4**	**4**	**3**	**5**	**4**	**3**	**3**	**3**	**5**	**5**	**5**
Heat Output	0	3	5	4	1	1	1	4	3	3.5	3	3	3
Reaction Time	**0.15**		**5**	**5**		**1**	**1**		**1**	**1**		**5**	**5**
Robustness	0		5	5		1	1		3	3		1	1
Maintenance	0		5	5		1	1		3	3		4	4
Safety	0		5	5		3	3		4	4		1	1
Area / Distance	**0.1**	**3**		**3**	**4**		**4**	**5**		**5**	**4**		**4**
Score	**1**	**3.8**	**2.75**	**4.55**	**3.05**	**1.6**	**3.35**	**3.35**	**1.5**	**3.5**	**2.25**	**2.4**	**2.9**

In summary, we have established that from the literature and experts in the field, the proposed light structure is diffuse dome/flat due to the glinting/glare and shadow reduction properties, and the proposed source is from LEDs due to their output stability, on-time, intensity, reaction time and work area/distance.

2.2 PHYSICS

Before delving onto the control, some metrics of lighting need to be highlighted. Measurement of light is possible through different techniques resulting in different representations of the light and metrics. Luminous Intensity (Candela) represents the amount of light emitted in the range of a three-dimensional angular span (Figure 7). Since the angular span is constant regardless of the source's distance, the luminous intensity is equal for surfaces A and B in Figure 7.

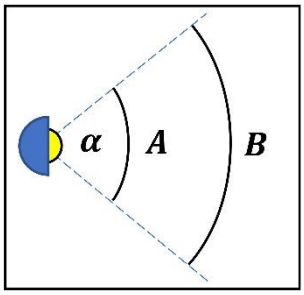

Figure 7: Luminous intensity angular span

This is a property of the light source found in the data sheets [27, 28]. If the luminous intensity is not included in the datasheet, the aforementioned angular span is provided in its place and used to calculate the luminous intensity. The angular span is measured in steradians (solid angle, Ω). Similar to radians, steradians are unit-less, and 1 steradian in a sphere of 1 m radius would produce a surface area of 1 m^2, which indicates that the said sphere would have 4π steradians. This angle is calculated using the light source's apex angle (α) through:

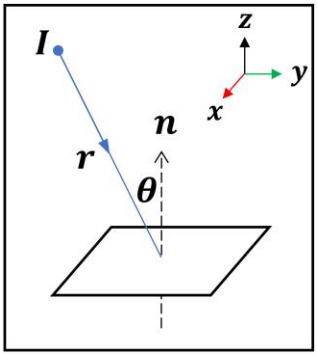

Figure 8: Luminous intensity to Illuminance relation

$$\Omega = 2\pi\left(1 - cos\left(\frac{\alpha}{2}\right)\right) \quad 2.1$$

Where Ω is the solid angle, α is the apex angle, I is the luminous intensity, and L is the luminous flux. Here, luminous flux (lumens) represents the light's amount of energy. Taking the luminous flux and the solid angle defined earlier, one can calculate the luminous intensity through [27, 28]:

$$I = \frac{L}{\Omega} \quad 2.2$$

The final critical property is illuminance which is measured in Lux. This is a measure of the illumination of a surface instead of that of an angle. This measurement is the easiest to understand and to compare since it is affected by the angle of incidence of the light (θ) and the distance between the source and surface (r) (Figure 8). The more distant the surface is from the source or the larger the angle of incidence, the less the illumination [27, 28]. As in Figure 9, it is clear that surface A has greater illuminance values than that of B. Illuminance at a single point on a surface is calculated using the following relationship [27, 28]:

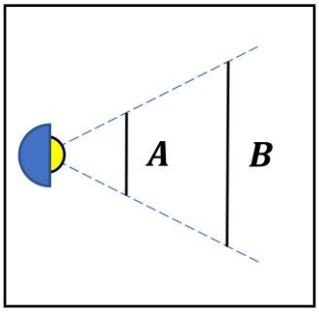

Figure 9: Illuminance on surfaces

$$E = \frac{I \cos\theta}{r^2} \tag{2.3}$$

To calculate the illuminance at a point on a surface from several light sources (n), the equation is generalized to include a summation based on the number of light sources, resulting in equations

$$E = \frac{I_i \cos\theta_i}{r_i^2} \tag{2.4}$$

$$E = \sum_{i=1}^{n} \frac{I_i \cos\theta_i}{r_i^2} \tag{2.5}$$

Combining the multiple lights equation (2.5) and selecting LEDs as the source, a WS2812B [29] 8×8 light mesh was procured. A control circuit and RGB chip are integrated into each unit of the 8×8 grid, allowing each unit to be addressed and have independent brightness and color control. The luminous intensity data was extracted, as shown in Table 2, and used in the calculations from the datasheet of the purchased LEDs. Since the LEDs are a combination of three smaller RGB LEDs, each source has its luminous intensity range.

Table 2: WS2812B Datasheet Luminous Intensity

Color	Model	Wavelength (nm)	Luminous Intensity (mcd)	Voltage (V)
Red	13CBAUP	620 – 630	550 – 700	1.8 – 2.2
Green	13CGAUP	515 – 530	1100 – 1400	3.0 – 3.2
Blue	10RIMUX	465 – 475	200 – 400	3.0 – 3.4

For the focused while-light illumination, to avoid using a spectrometer to identify the contribution of each color, we created a performance correction factor, C_l, that normalizes the weighted luminous intensity by:

$$I_i = C_l(R_{max} + G_{max} + B_{max}) = C_l(700 + 1400 + 400) = 2500C_l\ mcd = 2.5C_l\ cd \quad 2.6$$

where C_l and the maximum luminous intensity contribution of each color ($R_{max} = 0.7\ cd$, $G_{max} = 1.4\ cd$ and $B_{max} = 0.4\ cd$) are used to approximate the 8×8 light source's final capabilities. We used experimentation to derive the performance correction factor by installing the lights at a measured elevation above a work-surface and by comparing the calculated illuminance E_c using equation 2.5 with the measured illuminance E_a at a given point. The performance correction factor is calculated via:

$$C_l = \frac{E_a}{E_c} \quad 2.7$$

Further generalizing the equation to cover any point in the work-space, the notation $(i|j)$ is introduced to represent the relative position of the light sources (i) to the point being studied (j):

$$E_j = \sum_{i=1}^{n} \frac{I_i \cos\theta_{(i|j)}}{r^2_{(i|j)}} \quad 2.8$$

Putting it into matrix form yields our geometric model of multi-source lighting. Where m represents the number of points on the desired surface and n is the number of light sources being controlled. The illuminance matrix E is $m \times 1$, the A matrix is $m \times n$, and the luminous intensity matrix I is $n \times 1$.

$$\begin{bmatrix} E_1 \\ \vdots \\ E_m \end{bmatrix} = \begin{bmatrix} \frac{\cos\theta_{(1|1)}}{r^2_{(1|1)}} & \cdots & \frac{\cos\theta_{(1|n)}}{r^2_{(1|n)}} \\ \vdots & \ddots & \vdots \\ \frac{\cos\theta_{(m|1)}}{r^2_{(m|1)}} & \cdots & \frac{\cos\theta_{(m|n)}}{r^2_{(m|n)}} \end{bmatrix} \begin{bmatrix} I_1 \\ \vdots \\ I_n \end{bmatrix} \quad 2.9$$

Chapter 3. ADAPTIVE LUMINOUS INTENSITY

With the selection of our lighting methodology, source, and understanding of the photometry of lighting, we come to our first feature in the controlled environment, Adaptive Luminous Intensity. Since illuminance is the property that shall be used to describe the quantity of lighting on a surface, the measure of said property is crucial.

3.1 SENSOR

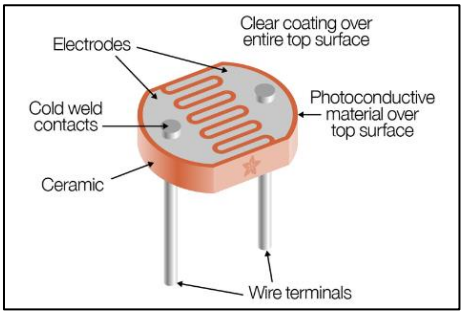

Figure 10: Labeled LDR

There are several light sensing systems including photo-emissive cells, photo-conductive cells, photo-voltaic cells and photo-junction devices. For this work, a photo-junction-based sensor is used for the benefits of its low cost and the continuous nature of its readings instead of on-off outputs of photo-diodes. Light Dependent Resistor (Figure 10 [30, 31]) (LDR) (Photo-conductive Cell) are active components that decrease in resistance with respect to incident light. The range of resistance outputs varies from several megaohms in dark conditions to hundreds of ohms under direct bright light [32]. Hence LDRs are usually assembled as a voltage divider circuit to capitalize on the variable resistance property. Furthermore, Figure 11 shows the

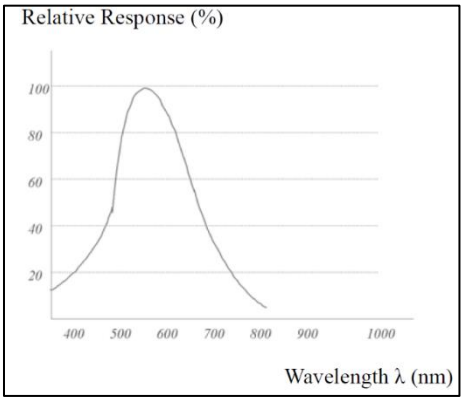

Figure 11: LDR relative response

wavelength response of the LDR extracted from the LDR data sheet (White Light 380-700 nm) [32]. This response curve was taken into consideration in the process of selecting both the light source and light meter. To utilize the LDRs, the characteristic behavior is required to convert the instantaneous variable resistance into variable illuminance. To accurately and easily measure illuminance a suitable Light Meter must be used to handle the spectrum of lighting selected for the job. Since the focus is with visible light emitted through LEDs, the Extech LT-45, which allows measurements of white, red, green, and blue LEDs, fluorescent, incandescent, and halogen lights [33] is chosen. Furthermore, the meter is programmed to compensate using color correction factors [33] (Table 3).

Table 3: Color correction factors

Light Source	C_c
Incandescent	1.010
White LED	0.915
Amber LED	1.024
Green	0.849
Red	1.953
Blue	1.475

Figure 12 [33] shows the wavelength response of the light meter, extracted from its datasheet. The data overlaps the behavior of the LDR to an acceptable extent, and taking into consideration the color correction factors that would improve the extrema matching for low and high wavelengths, the meter is suitable for our task. If higher accuracy readings or a larger spectrum of lighting are required, an optical spectrometer is recommended. These characteristics were extracted from the data sheets of six LDR models and subjected to a known illuminance value of approximately

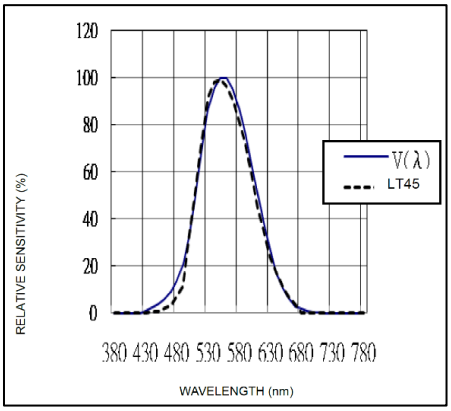

Figure 12: Light meter response curve

12,000 Lux (measured by a calibrated Lux meter), and the consequent LDR resistance was converted into an illuminance reading. The results are shown in Table 4, where it is clear that none of the datasheet characteristic behaviors of any models could replicate the calibrated Lux meter reading.

Table 4: LDR Data-sheet Characteristic Verification

Model	Desired Lux	Measured Lux
GL5506	12,098.30	2,636.73
GL5516		2,586.31
GL5526		9,029.66
GL5528		6,128.79
GL5537		34,136.14
GL5539		51,527.30

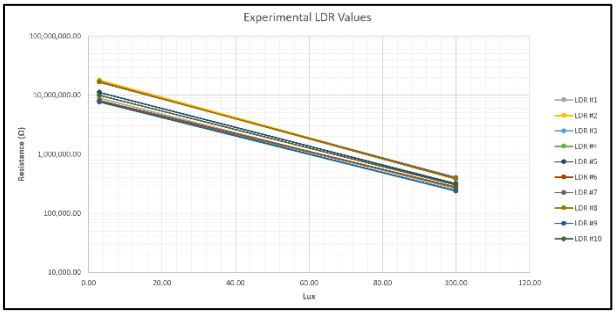

Figure 13: Experimental LDR performance

To test the validity of the characteristic plots [32] further, we designed an experimental setup. Out of each LDR model, 10 were selected and tested through the procedure outlined in 3.1.1 up to point 3. Each of the 10 LEDs from each model had 2 measurements taken, at a high illuminance value and one at a low illuminance value; Figure 13 and Figure 14 are of the model GL5539. The first graph represents 20 readings (2 for each LDR) plotted on a Log/Log grid to show the inconsistency and unreliability highlighted in the data sheets where the behaviors were visualized as regions in the grid rather than a single line. The maximum and minimum values at both ends were plotted against the values extracted from the datasheets and plotted on a single

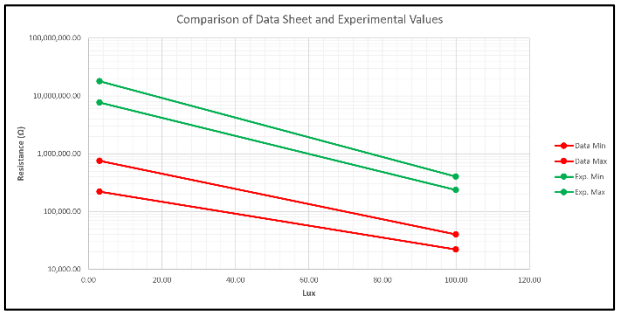

Figure 14: LDR performance experimental and datasheet comparison

Log/Log grid. As shown in the second plot, the red lines represent the bounds of the datasheet values, and the green lines represent the values gathered from the experimental results. This plot further highlights the unreliability of the LDR data sheets as benchmarks for performance. Therefore all LDR's used should be calibrated. The relationship between illumination and resistance is logarithmic;

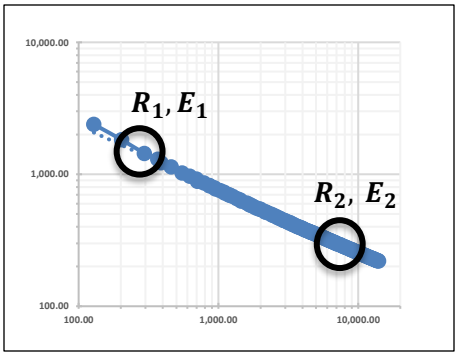

Figure 15: LDR logarithmic relationship

therefore, the line becomes straight when plotted on a logarithmic scale (Figure 15). Below is the derivation process of an LDR characteristic equation from the logarithmic Resistance against Illuminance relationship [34]. Through extracting R_1, E_1 and R_2, E_2 which represent the resistance and lux values at a low lux and high lux level respectively, one can establish a relationship between any point along the line (R_{LDR}, E_{LDR}) by relating the gradients of the logarithmic relationship which is represented as follows:

$$\frac{\log R_{LDR} - \log R_1}{\log E_{LDR} - \log E_1} = \frac{\log R_{LDR} - \log R_2}{\log E_{LDR} - \log E_2} \tag{3.1}$$

Combining the terms associated to $\log R_{LDR}$ yields

$$\log R_{LDR}\left(\frac{1}{\log E_{LDR} - \log E_1} - \frac{1}{\log E_{LDR} - \log E_2}\right) = \frac{\log R_1}{\log E_{LDR} - \log E_1} - \frac{\log R_2}{\log E_{LDR} - \log E_2}$$

$$\Leftrightarrow \log R_{LDR}\left(\frac{\log E_{LDR} - \log E_2 - \log E_{LDR} + \log E_1}{(\log E_{LDR} - \log E_1)(\log E_{LDR} - \log E_2)}\right)$$

$$= \frac{\log R_1\,(\log E_{LDR} - \log E_2) - \log R_2\,(\log E_{LDR} - \log E_1)}{(\log E_{LDR} - \log E_1)(\log E_{LDR} - \log E_2)}$$

$$\Rightarrow \log R_{LDR}\,(\log E_1 - \log E_2) = \log R_1\,(\log E_{LDR} - \log E_2) - \log R_2\,(\log E_{LDR} - \log E_1)$$

$$\Rightarrow \log R_{LDR} = \frac{\log R_1\,(\log E_{LDR} - \log E_2) - \log R_2\,(\log E_{LDR} - \log E_1)}{(\log E_1 - \log E_2)}$$

$$\Rightarrow \log R_{LDR} = \log E_{LDR}\left(\frac{\log R_1 - \log R_2}{\log E_1 - \log E_2}\right) + \frac{\log R_2 \log E_1 - \log R_1 \log E_2}{\log E_1 - \log E_2} \quad 3.2$$

Two constants, K and M, are defined to describe the behavior of the LDR for simplicity purposes allowing for the derivation of any Lux or Resistance value given the other [34]:

$$K \triangleq \frac{\log R_1 - \log R_2}{\log E_1 - \log E_2} \quad 3.3$$

$$M \triangleq \frac{\log R_2 \log E_1 - \log R_1 \log E_2}{\log E_1 - \log E_2} \quad 3.4$$

Then equation 3.2 becomes

$$R_{LDR} = 10^{K \log E_{LDR} + M} \quad 3.5$$

$$E_{LDR} = 10^{\frac{\log R_{LDR} - M}{K}} \quad 3.6$$

Both equations were used in the LDR calibration process and the control system for lighting consistency, as we shall now discuss in details.

3.1.1 *Calibration Procedure*

1. A light source, as per section 2.2, is fixed at a measured elevation above a work-surface. The expected light illuminance at a given point is calculated (E_c) using equation 2.5, and the actual subsequently measured (E_a) at the same elevation and point to calculate the light performance correction factor (C_l) using equation 2.7.
2. The LDR is connected to a multi-meter/ohmmeter to measure its resistance.

3. A light meter is placed at the LDR's elevation to assure consistency in readings. However, if there are constraints such as the size of the sensor or light meter probe, the following is recommended:

   a. A reference point is selected, preferably at a corner in the work-space (Figure 16).

   b. From the reference point, the x, y, and z coordinates are measured for both the Light Meter and sensor, (x_m, y_m, z_m) and (x_s, y_s, z_s) respectively (Figure 17).

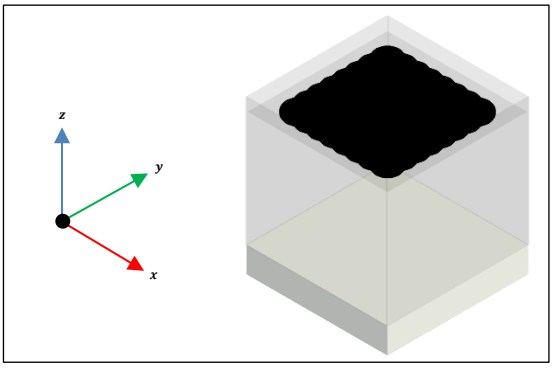

Figure 16: Modelled workspace

   c. The coordinates are to be input into the MATLAB code in Appendix B which has the aforementioned lighting model in section 2.2 calculating the Lux levels at both locations (E_m and E_s), from which a positional correction factor (C_p) is derived using the equation

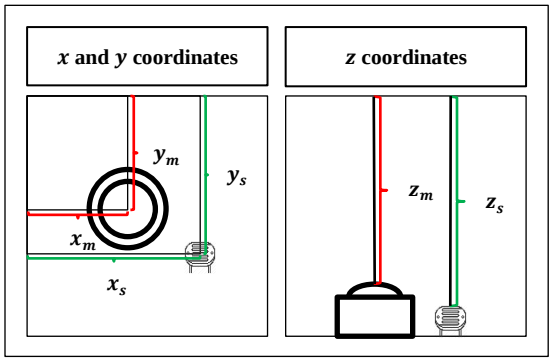

Figure 17: Measurement methodology

$$C_p = \frac{E_s}{E_m} \tag{3.7}$$

   d. In addition to C_p, a second correction factor is required, which is related to the type of Light Meter being used, the color correction factor (C_c).

4. The brightness of the installed light source is varied, and both Lux and Resistance readings are recorded.

5. Both C_p and C_c are multiplied by the illuminance readings of the meter E_m to convert it to the level, position, and lighting of illuminance readings at the sensor.

6. The collected data is plotted on both Normal and Logarithmic Scales to confirm LDR logarithmic linearity. After confirmation, there two possible approaches:
    a. Using equations 3.3 and 3.3, the K and M constants are derived for several intervals along the Data then averaged out.
    b. A best fit exponential relationship is derived to closely represent the relationship from which the K and M constants are derived.
7. Upon Calculating the Characteristic Constants of the LDR K and M, equation 3.5 is used to calculate the relative resistance of the LDR from the recorded Lux values and plotted against the experimental data to ensure correlation.

3.2 CONTROL SYSTEM

With the lighting and sensing system selected and calibrated, an assembly of the system is required with a controller to maintain consistent lighting in the work-space. Figure 18 shows the proposed design of the work-space, where the three main components are the LED light source, the LDR sensing medium, and an Arduino controller selected for simplicity and ease of programming. Capitalizing on the calibrated LDR and its inherent behavior, a voltage divider is constructed, and the voltage across the LDR was fed into one of the analogs to digital converter ports in the Arduino board. The two ports of the voltage divider were connected to the ground and the Arduino 5-volt supply. The light supply is connected to one of the PWM generator pins, an external power supply, and the ground. The resistance of the

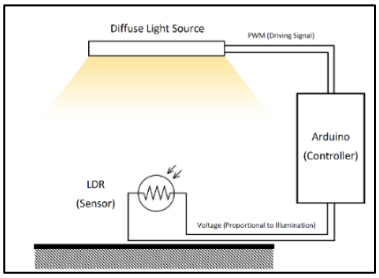

Figure 18: Design strategy

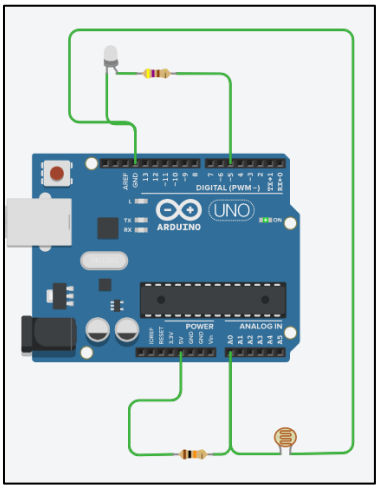

Figure 19: Controller and wiring

divider resistor should be selected based upon the operational range of the LDR. Specifically so the resistance of maximum illuminance should be much lower than the divider (at least 1: 10), and the resistance of minimum illuminance should be much higher than the divider (at least 10: 1). The LDR's instantaneous resistance is calculated using the equation for a voltage divider:

$$V_o = V_{in}\frac{R_{LDR}}{R_{LDR}+R_{Div}} \quad \Rightarrow \quad R_{LDR} = \frac{R_{Div}V_o}{V_{in}-V_o} \tag{3.8}$$

Where V_o is the Voltage Out, V_{in} is the Voltage In, R_{LDR} is the Resistance of LDR, and R_{Div} is the divider resistance. Following this, the Arduino analog pin measurements are used to calculate the LDR instantaneous resistance using equation 3.8 and substituted in equation 3.6 to calculate the incident illuminance at the LDR. The calculated illuminance was compared to the desired illuminance levels, and the light source then supplies the difference. Since the LDR is an analog sensor and noisy due to its sensitivity, a low pass filter is applied to the analog to digital converter pin to avoid unwarranted variations in the supplied lighting. A PID controller was used to eliminate steady-state error and allow for a smooth transient response. Figure 20 below shows the preliminary block diagram of the proposed control system.

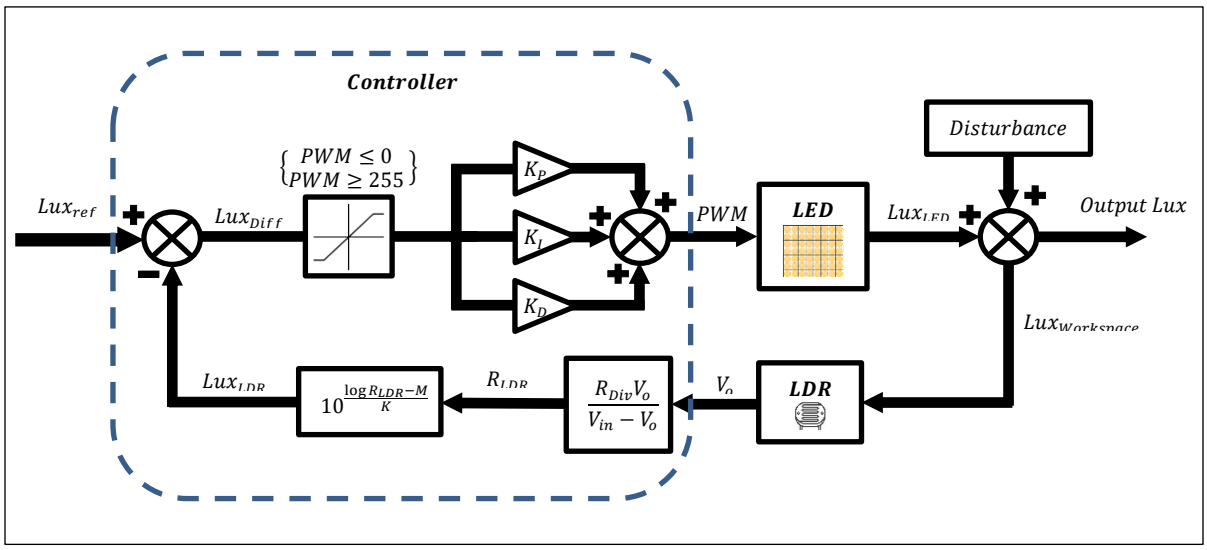

Figure 20: System block diagram

Proceeding forward to gain full capability of tuning the PID, two approaches were taken after the calibration process is complete; each outlined below:

1. Mathematical modeling using component data sheets
2. System identification + mathematical modeling using component data sheets

The applied illuminance disturbance is in the shape of a square wave with a magnitude of 500 Lux and a reducing period from 10 seconds to 0.002 seconds.

3.2.1 *Modeling*

Datasheet Based model

The characteristic properties of the components installed in the system are extracted from their relative datasheets. LDR datasheet shows a Rise time of $20 - 30\ ms$ and a Fall time of $30\ ms$ [32], allowing the LDR to be modeled, in a first-order approximation, as a first-order differential equation using the rise time to calculate the time constant a. The corresponding transfer function is thus:

Specification	Light resistance (10Lux) (KΩ)	Dark resistance (MΩ)	γ_{10}^{100}	Response time (ms)		Illuminance resistance Fig. No.
				Increase	Decrease	
Φ5 series	5-10	0.5	0.5	30	30	2
	10-20	1	0.6	20	30	3
	20-30	2	0.6	20	30	4
	30-50	3	0.7	20	30	4
	50-100	5	0.8	20	30	5
	100-200	10	0.9	20	30	6

Figure 21: LDR datasheet response times

$$\frac{E_r(s)}{E_i(s)} = \frac{a}{s+a} \quad ; \quad a = \frac{2.2}{0.03} = 73.33 \tag{3.9}$$

The LED datasheet indicates a Transmission Delay of $300\ ns$ and a Fall time of $120\ \mu s$ [29]. These are modeled as a time delay in the system model. First, a setpoint or desired illuminance level was set using the calibrated LDR K and M

Switching characteristics (T_A=-20～+70℃, V_{DD}=4.5～5.5V,V_{SS}=0V,unless otherwise specified)

Prameter	Symbol	Condition	Min	Tpy	Max	Unit
Transmission delay time	t_{PLZ}	CL=15pF,DIN→ DOUT,RL=10KΩ	——	——	300	ns
Fall time	t_{THZ}	CL=300pF,OUTR/OUTG/OUTB	——	——	120	μs
Input capcity	C_I	——	——	——	15	pF

Figure 22: LED datasheet response times

constants. For simplicity and confirmation, a percentage of the maximum LED capabilities given the properties and position of LDR respective to the source was used for the desired disturbance and noise values. The desired value was converted into the candela value of the light source through equation 2.8, which is then converted into a PWM duty cycle signal and saturated between 0 and 1, and fed into the LED block (Figure 23).

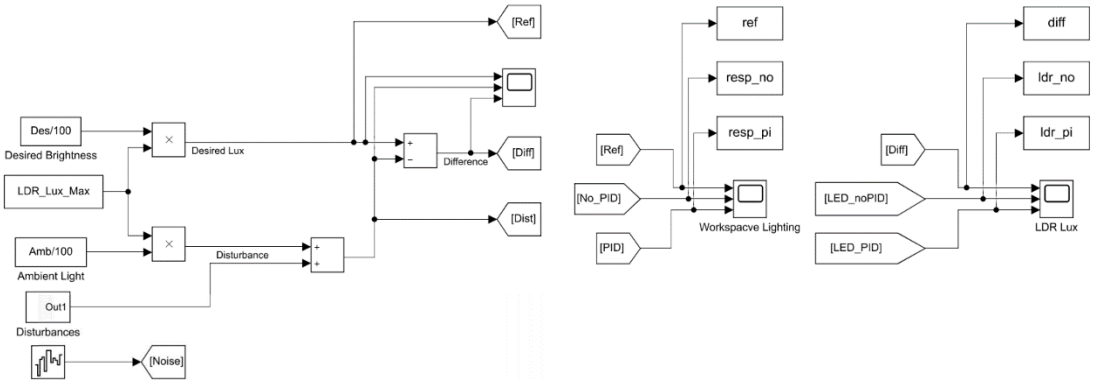

Figure 23: Simulink model inputs and outputs

The derived transfer function representing the LDR behavior (3.9) is used to construct the plant. Additionally, a low pass filter is physically employed due to the high sensitivity of LDR's. The remainder of the system is constructed to be in line with the system block diagram (Figure 24).

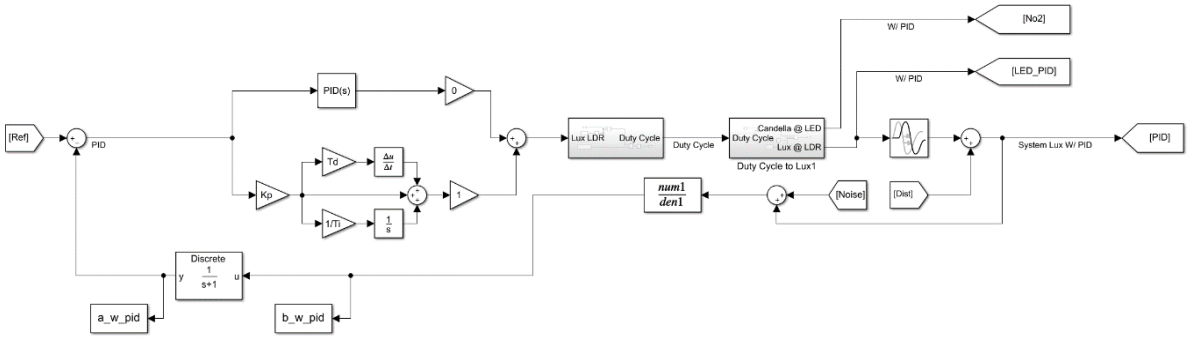

Figure 24: Simulink Mathematical Model

The PID controller was tuned to assure a unity DC gain and to minimize oscillation below the operation bandwidth. The results are shown in Figure 25. The plots are separated into two sets:

the first row represents the first five seconds of the response, whereas the second covers fifty seconds of the response. The first column is the work-space overall illuminance (measured by the LDR), and the second represents the LED contribution output to the illuminance. The lights are observed to compensate successfully for the noise and changing external disturbance. The tuned controller values were applied to the constructed physical system, and the results are highlighted in section 5.1.

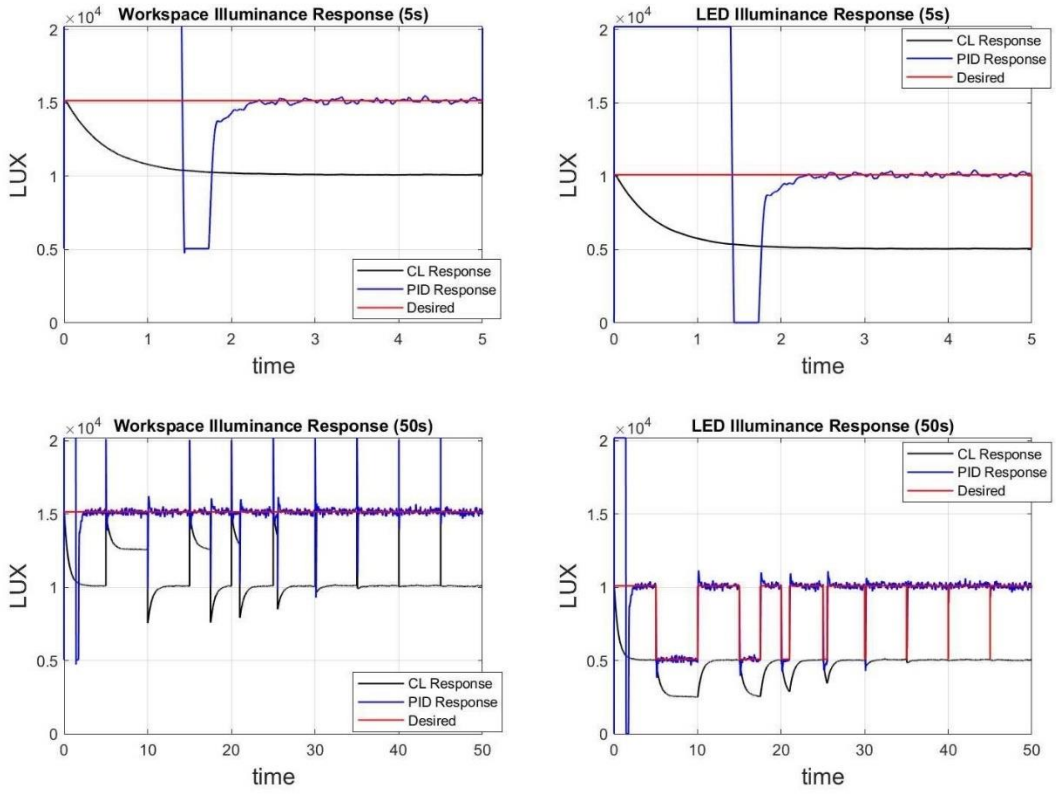

Figure 25: System Responses based on first-order approximate Model

System Identification

Following the same methodology outlined for the noise, disturbances, desired value, and LEDs of the mathematical model, system identification is constructed to increase fidelity of the plant model (Figure 26). The setup outlined in section 3.1.1 was utilized along with the calibrated LDR in writing a script that excited the LEDs with a PRBS using an 11^{th} order monic polynomial (pseudo-

random binary sequence $x^{11} + x^9 + 1$) with a 2,047-bit sequence at a sampling rate of 250 Hz, which is approximately an eighth of the rise time of the LDR (30 ms) to ensure a proper capture of the frequency response.

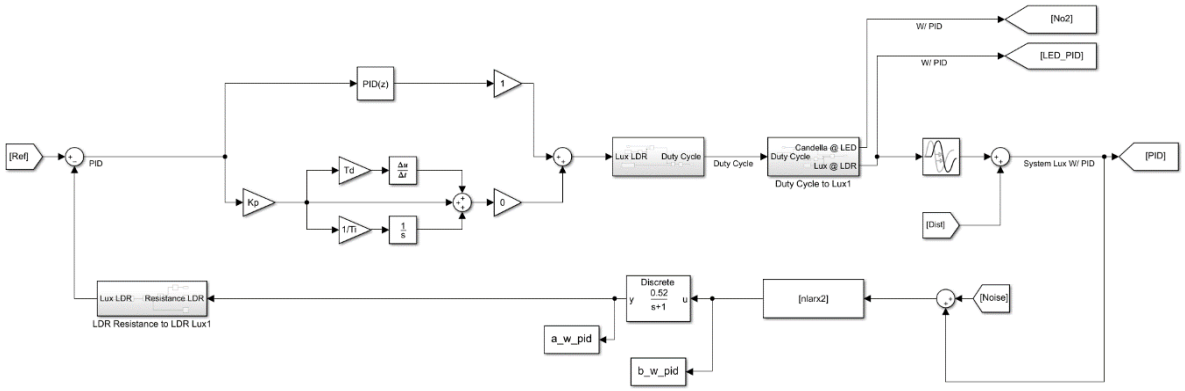

Figure 26: Simulink System Identification Model

The output resistance of the LDR is measured at 250 Hz and recorded using the serial output of the lighting controller, and input into the system identification toolbox in MATLAB. After model tuning, and a nonlinear neural network is derived (Figure 27).

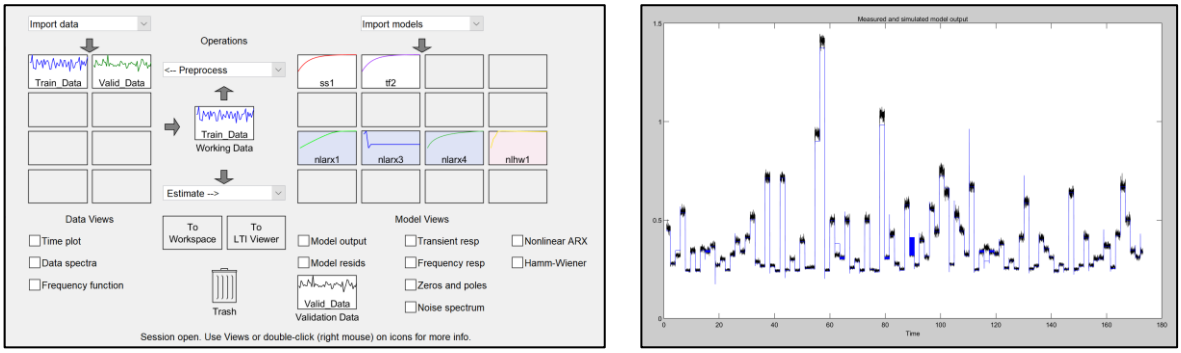

Figure 27: (1) Model tuning system identification toolbox (2) model matching

The resulting neural network matching is capable of recreating the validation data at 97% accuracy, and is imported into Simulink as the plant (Figure 26). The PID was tuned and yielded, the controlled illuminance in Figure 28. The plots are arranged similarly to Figure 25, and the proposed lighting is observed to compensate for the noise and external disturbances successfully.

Due to the included nonlinearity, the behavior is smoother and less noisy compared to the case with the analytic model. The tuned controller parameters are also applied to the constructed physical system, and the results are highlighted in section 5.1.

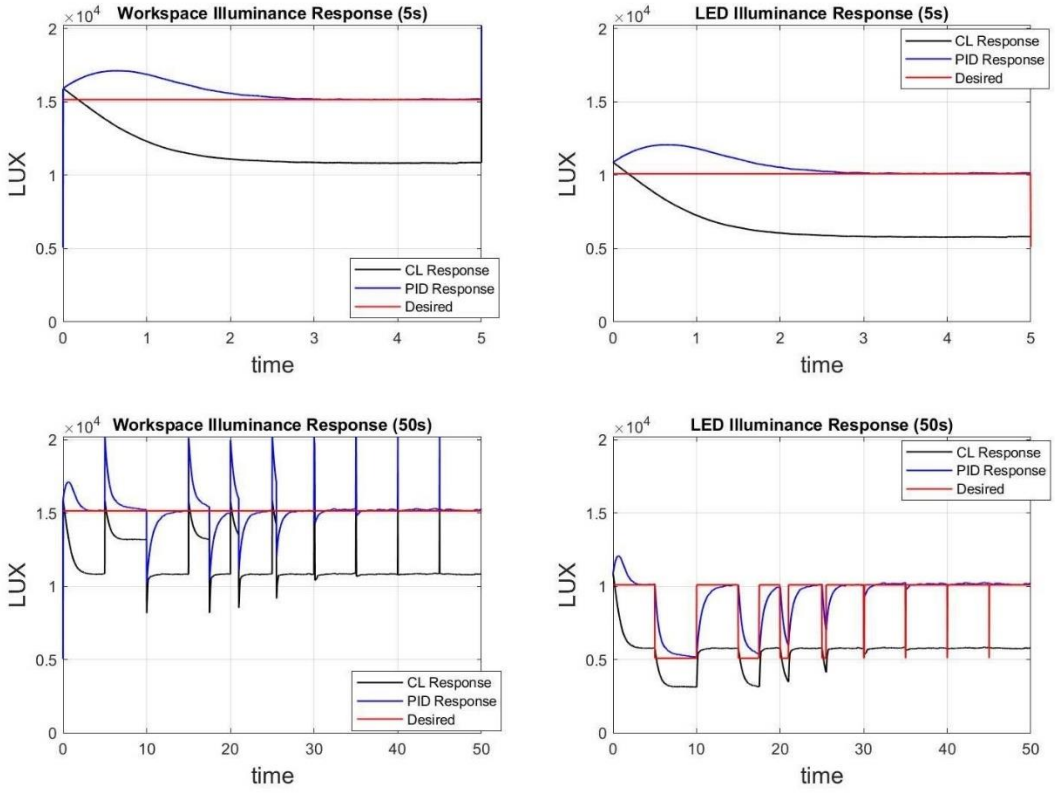

Figure 28: System Responses System Identification

Focusing on the work-space illuminance plots (to the bottom left) of Figure 25 and Figure 28, we observe that the illuminance level is indeed maintained with the proposed feedback control. The spikes observed are the result of the shifting disturbance of 500 Lux. In comparing both model behaviors, the system identification-based model is smoother in its behavior with significant noise reduction. However, the data-based model is not as responsive to small disturbance periods as the mathematical model. As can be observed, the mathematical model can recover from a

disturbance within 0.5 seconds, whereas the system-identification takes 1.25 seconds to achieve the same level of disturbance attenuation.

Chapter 4. ADAPTIVE ILLUMINANCE DISTRIBUTION

In this chapter, we look into the surface topography considerations and compensation, which is a Novel approach, specifically the adaptive illuminance distribution. We further develop illuminance equation 2.9 to develop a system to control the surface lighting over flat and curved surfaces and seek high-fidelity simulations to gain further insight into surface lighting control.

4.1.1 *Proof of concept*

Denoting equation 2.9 in the form $E = AI$ and noting that m is usually much larger than n, we can solve for the luminous intensity vector I with the method of least-squares:

$$I \approx (A^T A)^{-1} A^T E \tag{4.1}$$

However, since the lights luminous intensity is limited (I_{max}), a box constrained least-squares was used, allowing for physically valid solutions. A convex optimization problem is derived and solved through the Interior-point method:

$$I = \min_I \frac{1}{2} \|AI - E\|_2^2 \quad ; \quad s.t. \quad \{0 \leq I_i \leq I_{max}\} \tag{4.2}$$

This form enables taking an illuminance distribution as the input to produce the luminous intensity and structure of the different light sources required to supply the desired distribution. To illustrate the solution's validity, we developed a benchtop system in a smaller work-space (Figure 29 (1)). The controllable lights were fixed at a leveled height off a flat surface, and the coordinates of the lights in relation to a local coordinate system were recorded. This process was executed in the absence of ambient lights to avoid external disturbances and emphasize the least-squares solution's validity.

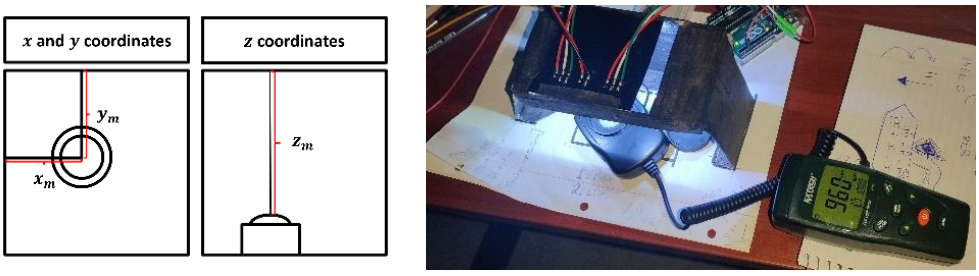

Figure 29: (1) Measurements (2) Experimental Setup (Meter measuring 1,000 Lux)

Using the optimal solutions, two illuminance distributions were imposed. The first was a constant 1,000 Lux and the second a constant 5,000 Lux over the full surface in the coordinate system. The calculated light source luminous intensities and structure were input into the lighting controller (Figure 30 (1) and (3)), and the illuminance of the surface was measured at random locations across the part surface (Figure 30 (2) and (4)).

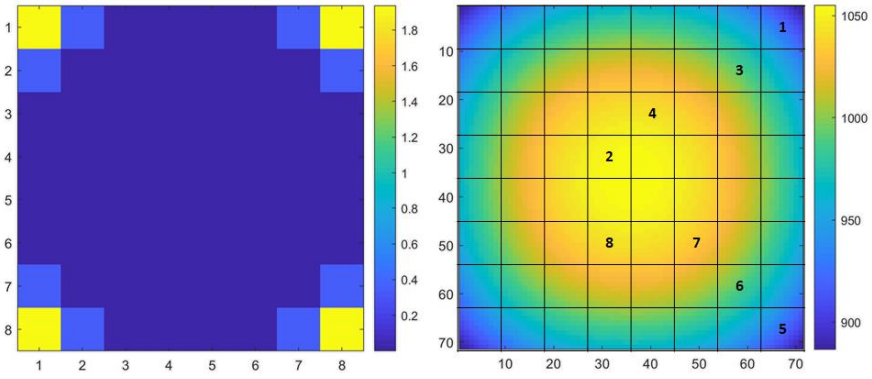

Mean = 998 ; Std. Dev. = 37 ; Abs. Mean Error = 31

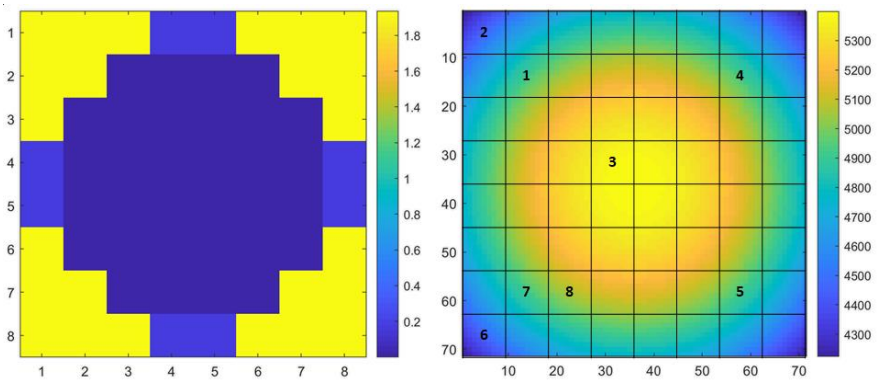

Mean = 4,983 ; Std. Dev. = 260 ; Abs. Mean Error = 218

Figure 30: Least Squares 1,000 Lux [(1) Intensity (2) Illuminance]

5,000 Lux [(3) Intensity (4) Illuminance

The experimental setup is shown in Figure 29 (2), where the 1,000 Lux solution is imposed, and the meter reads 960 Lux. The results of both settings are outlined in Table 5. As can be observed, the measured illuminance for the 1,000 Lux arrangement lies in the range 878 - 963 Lux, and the 5,000 Lux in the range 4,620 - 5,040 Lux. Hence, the concept of illuminance distribution control was proved for flat surfaces with an acceptable mean error of 7.9% (when targeting at 1,000 Lux) and 3.4% (when targeting at 5,000 Lux), and a standard deviation of 3% and 3%, respectively.

Table 5: Experimental confirmation of least-squares calculation

Point	**1,000 Lux**	**5,000 Lux**
1	878	4,930
2	963	4,620
3	914	5,040
4	961	4,960
5	887	4,800
6	906	4,680
7	916	4,720
8	941	4,980
Min.	878	4,620
Max.	963	5,040
Mean	921	4,841
Std. Dev.	30	147
Abs. Mean Error	79	169

These deviations arise because of the least-squares methodology and physical constraint of the lighting luminous intensity. In the next section, the strategy of expanding this to a three-dimensional surface is discussed.

4.1.2 *Extension to Uneven Topographies*

Accommodating three-dimensional surfaces required the extraction of the work-piece's position, geometry, and the calculated illuminance distribution. Since the work-piece is suspended in the

work-space, and has an uneven topography, accurate experimental measurement of lighting is very challenging due to the angle θ and distance r from each light source. Simulations were executed to further understand the behavior of illumiannce over a curved surface. We specifically used Autodesk Revit software with illuminance rendering capabilities and ease of orientation and control of the inter-spatial relationship between lights and work-piece. The work-space considered for the study, as per the selection process in section 2.1.3, was a $0.5m \times 0.5m \times 0.5m$ shooting tent with 120 base LEDs fixed at the top behind a diffuser. These components are all modeled in Revit as per Figure 31.

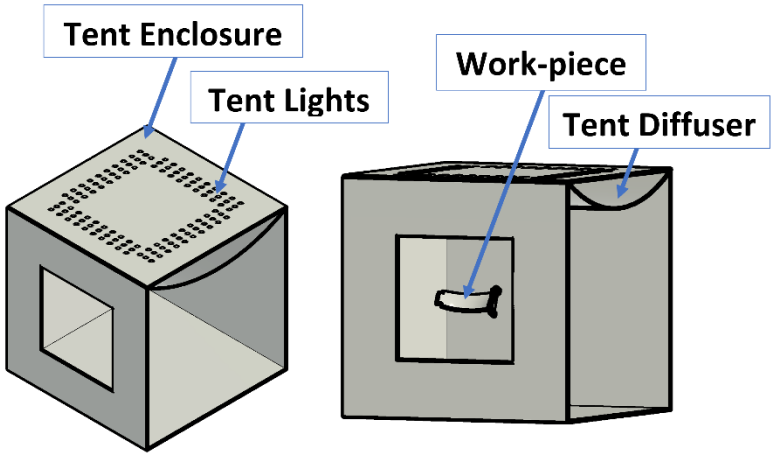

Figure 31: Work-space Autodesk Revit

Simulation Verification

We first verified the proposed high-fidelity simulation in Revit by benchmarking the physics-based calculations in the previous section. In Figure 32, the solution for the 1,000 Lux distribution on a flat surface was imposed from Figure 30 (1) and (2) inside the recreated work-space, and the results of the simulation are first compared with the experimentally measured results (Table 6). As Revit takes into into account reflective surface materials and light bouncing off walls only minor deviations from the physics-based calculation (mean error: 3.6%, standard

deviation: 6.7%) were witnessed. This observation verified the capabilities of Revit to produce accurate illuminance distributions.

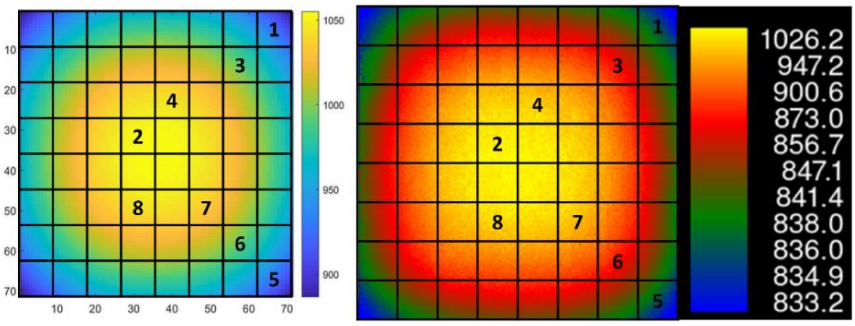

Figure 32: 1,000 Lux Illuminance Distribution
(1) Physics-based calculation (2) Revit high-fidelity simulation

Table 6: 1,000 Lux Measured vs. Simulation on Flat Surface

Point	Measured	Simulated
1	878	838
2	963	1,026
3	914	873
4	961	986
5	887	838
6	906	873
7	916	924
8	941	966
Min.	878	838
Max.	963	1,026
Avg.	921	916
Std. Dev.	30	67
Abs. Mean Error	79	36

The verification of uneven topography illuminance distributions compares the calculations to the Revit simulations due to the physical challenges highlighted earlier. First, 3D renditions of the work-space, lighting, and work-piece are constructed both in physics-based and high-fidelity Revit simulations. For the calculations, a discretized surface was used to calculate the illuminance over a finite number of points. The positioning of both is matched through

coordinate transformations based on the position and orientation of the workpiece in relation to the shooting tent. To calculate θ and r for each point on the work-piece surface, the angle between the surface normal and the vector between the light sources and point is calculated using the law of cosines. The position of the light sources ($n_{(x,y,z)}$), the work-piece and surface normal ($m_{(x,y,z)}$ and $M_{(x,y,z)}$) are imported as x, y, and z coordinates and used to calculate the angle $\theta_{(m|n)}$ and distance $r_{(m|n)}$ through:

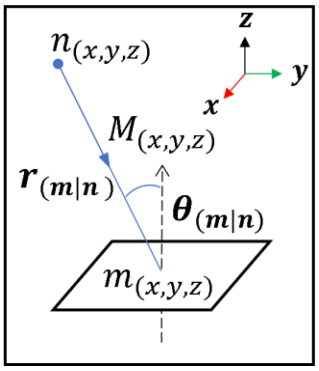

Figure 33: Luminous intensity to Illuminance relation

$$r_{(m|n)} = \left|M_{(x,y,z)} - m_{(x,y,z)}\right| \tag{4.3}$$

$$\theta_{(m|n)} = \cos^{-1}\left(\frac{\left|n_{(x,y,z)} - M_{(x,y,z)}\right|^2 - r_{(m|n)}{}^2 - \left|n_{(x,y,z)} - m_{(x,y,z)}\right|^2}{-2\left(\left|M_{(x,y,z)} - m_{(x,y,z)}\right|\right)\left(\left|n_{(x,y,z)} - m_{(x,y,z)}\right|\right)}\right) \tag{4.4}$$

In this work, we resorted to "Standard Triangle Language" (.stl) representations of the work-piece to extract both the surface and normal coordinates (Code in Appendix B). An optimal lighting distribution of 1,000 lux was imposed as E_m and the required I_n is calculated using equations 2.9, 4.2, 4.3, and 4.4.

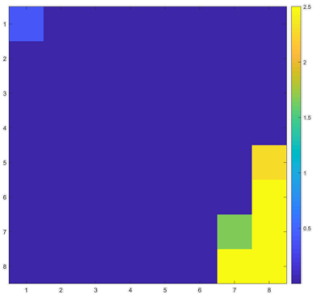

Figure 34: Imposed Luminous Intensity I_n for 1,000 Lux E_m

Figure 35 and Table 7. Figure 35 (1) represents the output of the calculations, while Figure 35 (2) shows the Revit illuminance simulation results. Extracting specific points from both yields the maximum and minimum illuminances in Table 7.

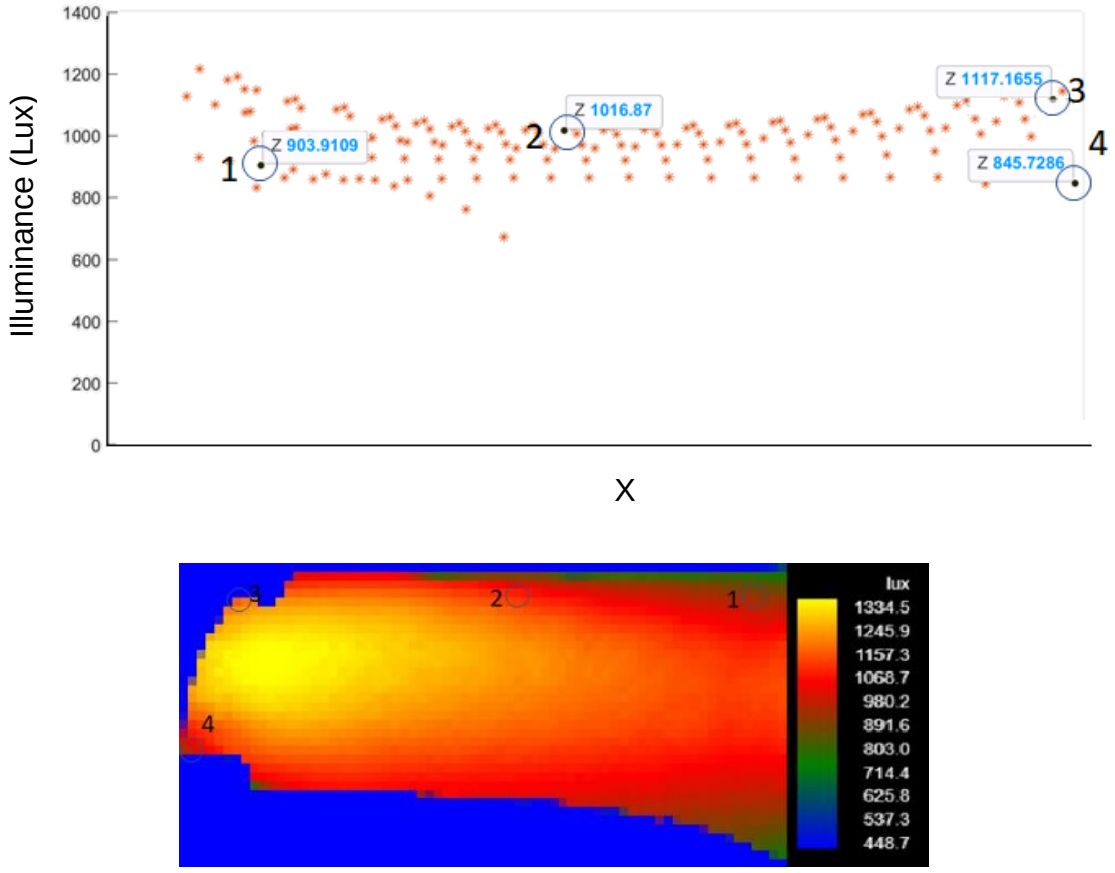

Figure 35: Illuminance Distribution E_m(1) Calculated (2) Simulated[2]

Table 7: Calculated vs. Simulated Illuminance E_m

Method	Min	Max	1	2	3	4
Calculated	673	1,216	904	1,017	1,117	844
Simulated	626	1,334	892	1,068	1,200	850

As we expect, a correlation was found with minor deviations due to Revit taking into account material reflections and bounce lighting. However, Table 5 illustrated the close correlation of the flat surface least-squares solution; this was due to the low granularity of the surface (5,400 points), whereas the 3D work-piece had a much higher granularity (324 points) which reduces

[2] Data has been intentionally pixelated and distorted

the calculation points and the accurate recreation of the surface. Another source of error is the work-piece placement in the work-space through Revit and the calculation software. The granularity of the surface is reduced significantly, and the placement of the work-piece is done through coordinate transformations to circumvent the highlighted limitations.

Simulation Insight

With the successful verification of Revit, the work-piece was exposed to different scenarios to extract valuable insights. The first insight is shown in Figure 36 below, where the illuminance distribution over the work-piece in Revit is compared to an actual captured image from the physical system.

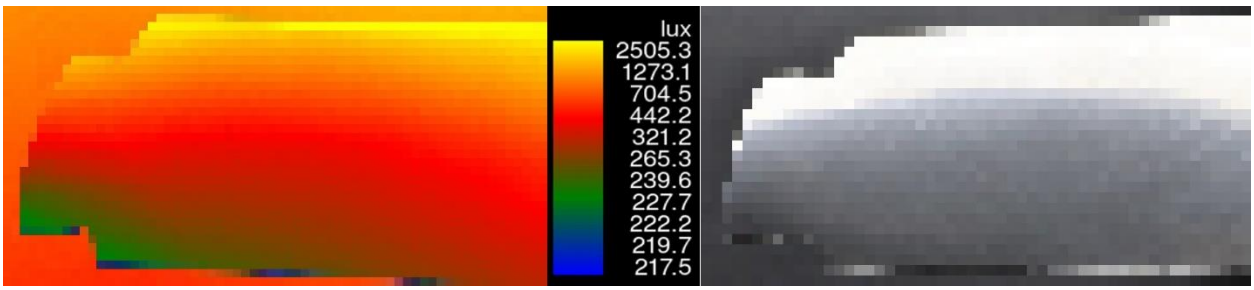

Figure 36: Glare/Gradient Comparison (1) Revit Simulation (2) Captured Image[3]

There is a clear correlation between the illuminance distribution in the simulation and the glare in the physically captured images. Glare is measured using the Unified Glare Rating (Discomfort Glare) [35, 36] and through contrast (Disability Glare) [37], both equations shown below. In both cases, there is a ratio between different levels of luminous flux.

$$UGR = 8\log\left[\frac{0.25}{L_b}\sum\left(\frac{L^2\omega}{p^2}\right)\right]$$

L = The Luminous Flux of the luminaire
L_b =The Luminous Flux the background

$$C = \frac{L_{max} - L_{min}}{L_{max} + L_{min}}$$

L_{max} = Maximum Luminous Flux
L_{min} = Minimum Luminous Flux

[3] Data has been intentionally pixelated and distorted

As illustrated in section 2.2, the luminous intensity I is directly proportional to the luminous flux L with a factor of $1/\Omega$ (equation 2.2). Thich is, in turn, proportional to the illuminance E using equation 2.3. Furthermore, different defect sizes and orientations were implemented on the work-piece with varying widths x and depths y (Table 8) in microns to visualize the interaction between the illuminance distribution and defect orientation, which could be parallel or perpendicular to the illuminance gradient.

Table 8: Modelled Defect Sizes

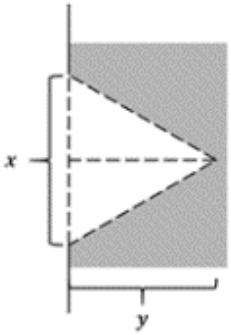

x (µm)	y (µm)	**Parallel**	**Perpendicular**
50	250	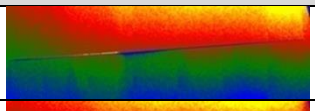	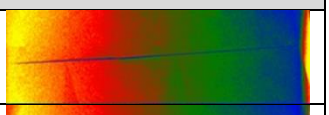
10	50	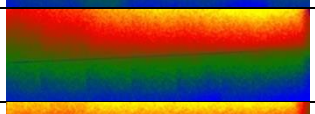	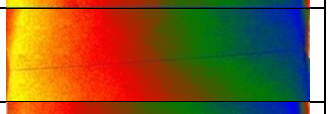
5	2.5		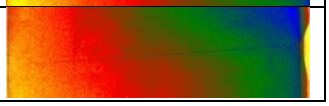

We observed a relationship between defect orientation and lighting gradient. As defect size decreases in the parallel orientation, so does the visibility of the defect. Whereas in the parallel orientation, the defect visibility is maintained through the decreasing defect sizes. Maintaining a consistent illuminance distribution over the surface will eliminate the dependence of defect orientation with respect to the gradient by increasing the contrast between lighting on the surface and within the defect. Therefore, from Figure 36 and Table 8, it is clear that a consistent illuminance distribution enforced on the inspection surface will ensure the elimination of glare and light gradients.

Proposed Strategy

The ability to maintain a consistent illuminance distribution was achieved by setting the desired illuminance over the work-piece surface ($[E]_D$), while considering the existing illuminance ($[E]_E$), to calculate the required compensation ($[E]_C$) that would balance the uneven existing distribution (Figure 37).

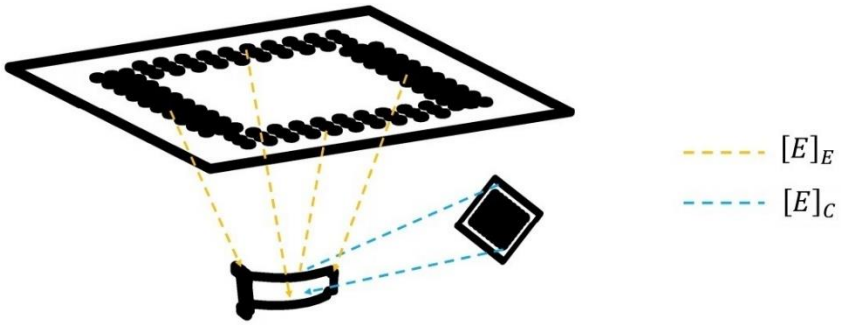

Figure 37: Strategy Outline

At the core of the multi-source lighting, we have the superposition:

$$\begin{bmatrix} E_1 \\ \vdots \\ E_m \end{bmatrix}_D = \begin{bmatrix} E_1 \\ \vdots \\ E_m \end{bmatrix}_C + \begin{bmatrix} E_1 \\ \vdots \\ E_m \end{bmatrix}_E \tag{4.5}$$

which yields the target compensation from the assistive lights:

$$\begin{bmatrix} E_1 \\ \vdots \\ E_m \end{bmatrix}_C = \begin{bmatrix} E_1 \\ \vdots \\ E_m \end{bmatrix}_D - \begin{bmatrix} E_1 \\ \vdots \\ E_m \end{bmatrix}_E \tag{4.6}$$

For the proposed LED array system, we have:

$$\begin{bmatrix} E_1 \\ \vdots \\ E_m \end{bmatrix}_C = \begin{bmatrix} \frac{\cos\theta_{(1|1)}}{r^2_{(1|1)}} & \cdots & \frac{\cos\theta_{(1|n)}}{r^2_{(1|n)}} \\ \vdots & \ddots & \vdots \\ \frac{\cos\theta_{(m|1)}}{r^2_{(m|1)}} & \cdots & \frac{\cos\theta_{(m|n)}}{r^2_{(m|n)}} \end{bmatrix} \begin{bmatrix} I_1 \\ \vdots \\ I_m \end{bmatrix} \tag{4.7}$$

Solutions of luminous intensity *I* can then be solved from the aforementioned model-based optimization in section 4.1.1.

4.1.3 *Solution by Boxed Least-Squares*

As highlighted earlier, the work-space has 120 base LEDs which represent $[E]_E$. Figure 38 shows the work-space, the 15 proposed positions for the work-piece to be inspected, the camera's line of sight, and the 120 LEDs.

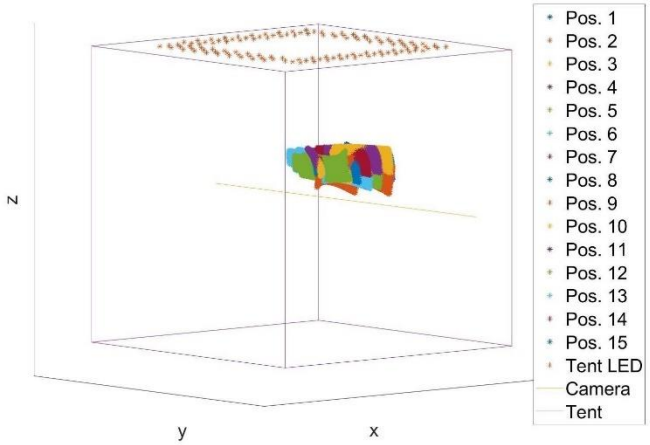

Figure 38: Work-space and Work-piece Placement

The positions are mapped using coordinate transformations by relating the CAD coordinate system I to the shooting tent coordinate system S (Figure 39).

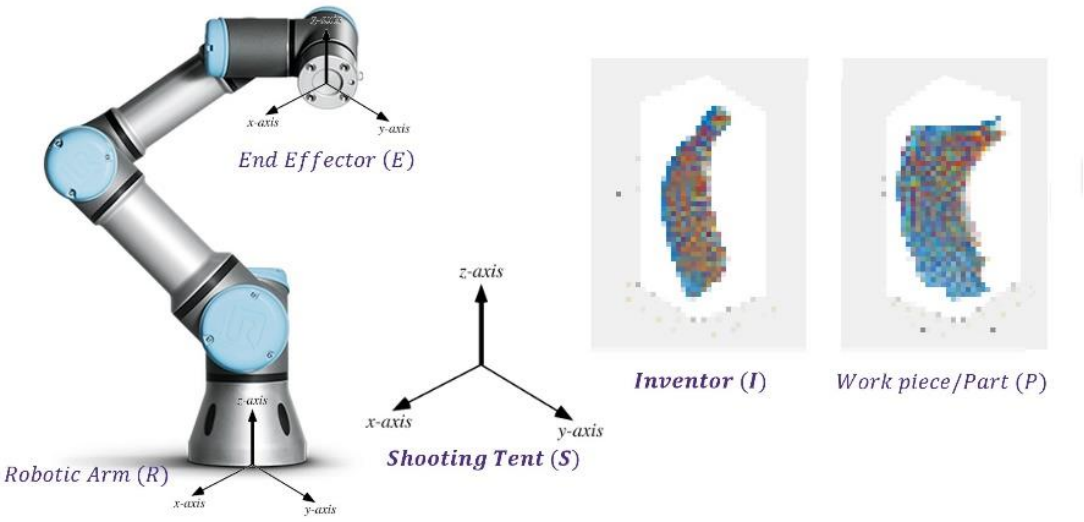

Figure 39: Coordinate systems[4]

[4] Data has been intentionally pixelated and distorted

This is achieved by transforming the CAD to part $[PI]$ to effector $[EP]$ to robot $[RE]$ and finally to the tent $[SR]$. Multiplying the transformations in order results in $[\boldsymbol{SI}]$ as per equation 4.8:

$$[\boldsymbol{SI}]=[SR][RE][EP][PI] \tag{4.8}$$

Since the work-piece is a 3D surface, the angle between the incident light and the surface normal is used as an indicator of inclusion in the calculation through conditioning the term $\cos\theta_{(i|j)}$, to avoid any negative contributions when the light ray enters from the back of the point of interest, i.e. when $\cos\theta_{(i|j)} < 0$ we assign $\cos\theta_{(i|j)} = 0$. Furthermore, as per section 4.1.2, the number of points was increased to 8,226 from 324. For a well-rounded comparison, five different configurations (C_0 - C_5) were considered for $[E]_D$. The mathematical representation of which is outlined below.

- Case C_0 : No Compensatory lighting is applied:

  $$[E]_D = [E]_E$$

- Case C_1 : Setting the max. value of $[E]_E$ as $[E]_D$, namely, we aim for uniform illuminance at the maximum environment condition:

  $$[E]_D = \max_E([E]_E)$$

- Case C_2 : Setting the max. value of $[E]_E$ in a sub-region (1/8) as $[E]_D$ and focus in this sub-region only:

  $$[E]_{D(s)} = \max_E\big([E]_{E(s)}\big)$$
  $$[E]_{D(\neq s)} = 0$$
  Where (s) denotes the subregion in question

- Case C_3 : Setting the max. value of $[E]_E$ in a sub-region (1/8) as $[E]_D$ and leave other regions unconstrained:

  $$[E]_D = \max_E\big([E]_{E(s)}\big)$$
  Where (s) denotes the subregion in question

- Case C_4 : Setting the max. value of $[E]_E$ in a sub-region (1/16) as $[E]_D$ and focus in this sub-region only:

  $$[E]_{D(s)} = \max_E([E]_{E(s)})$$
  $$[E]_{D(\neq s)} = 0$$
  Where (s) denotes the subregion in question

- Case C_5 : Setting the max. value of $[E]_E$ in a sub-region (1/16) as $[E]_D$:

  $$[E]_D = \max_E([E]_{E(s)})$$
  Where (s) denotes the subregion in question

Using the chosen $[E]_D$, the additional LED mesh contribution $[E]_C$ was calculated. Then using the proposed boxed least-squares, the required luminous intensity $[I]$ was calculated. An example of the least-squares solution is calculated for configuration C_1 in the work-piece's first position. First, the placement and orientation of both the compensatory lights and the work-piece are plotted inside the work-space (Figure 40 (1)). The existing illuminance distribution $[E]_E$ was calculated over the surface (Figure 40 (2)), following which the desired illuminance $[E]_D$ was derived based on the configurations mentioned above, and hence the needed compensatory illuminance $[E]_C$ (Figure 41 (1)), were derived.

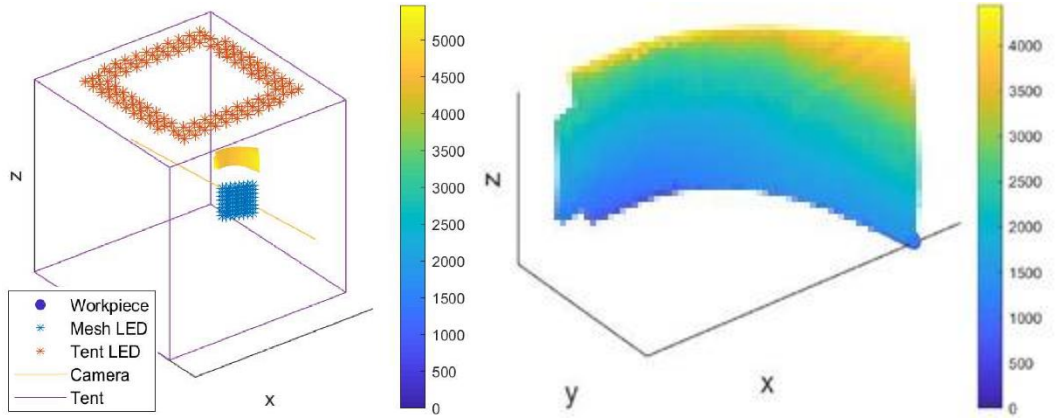

Figure 40: Illuminance of proposed adaptive illuminance distribution (1) Work-space Arrangement (2) Sections of Existing Illuminance $[E]_E$[5]

Figure 41 (2) presents the resulting optimal luminous intensity and structure of the LED arrays.

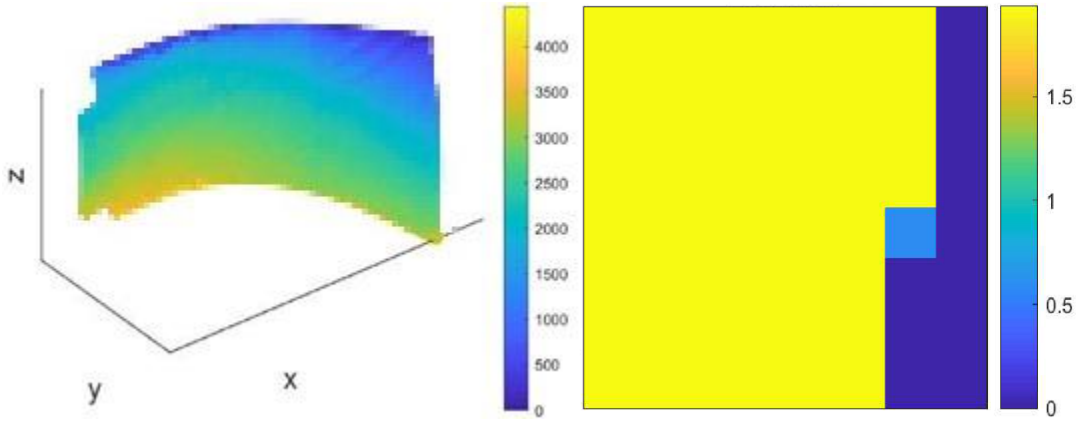

Figure 41: (1) Compensatory Illuminance $[E]_C$[5] (2) Least-squares Luminous Intensity $[I]$

The final illuminance distribution which is equivalent to $[E]_D$ is also plotted to ensure the compensation is achieved (Figure 42 (1) and (2)).

[5] Image does not scale; data has been intentionally distorted

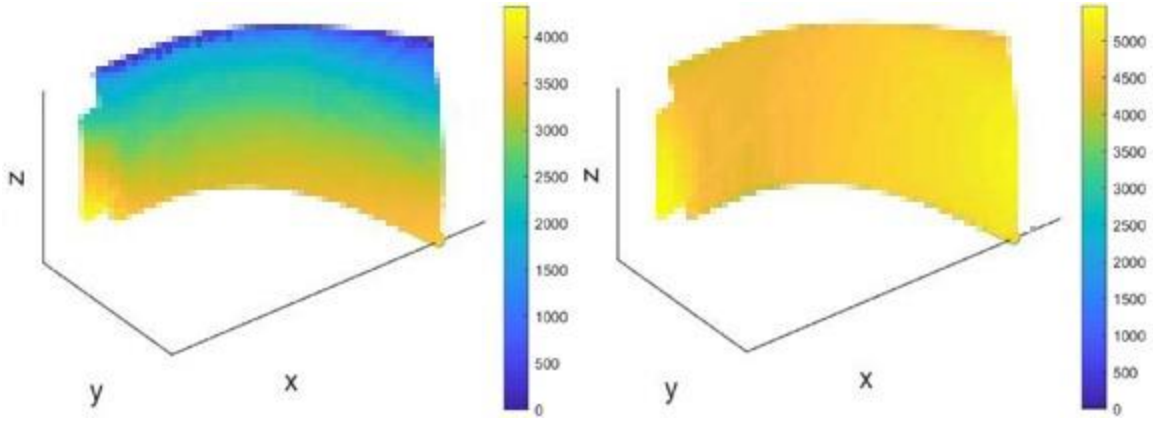

Figure 42: (1) Actual Compensation[6] (2) Final calculated Illuminance $[E]_D$

For this work, 15 solutions were derived, one for each work-piece position. These were programmed into the lighting controller to produce the optimal lighting shape for each position.

Chapter 5. RESULTS AND COMPARISON

5.1 ADAPTIVE LUMINOUS INTENSITY

The tuned PID values from section 3.2 were applied to the physical system and the performance recorded (Figure 43). The mathematical model's PID behavior is unsatisfactory due to significant steady-state error and noise (Figure 43 (1)). The system identification model's PID is much more successful at achieving the desired value with reduced but still significant oscillations (Figure 43 (2)). The system identification model values are fine-tuned and result in Figure 43 (3), which is observed to be very stable and successful at maintaining the desired value and void of noise.

[6] Image does not scale; data has been intentionally distorted

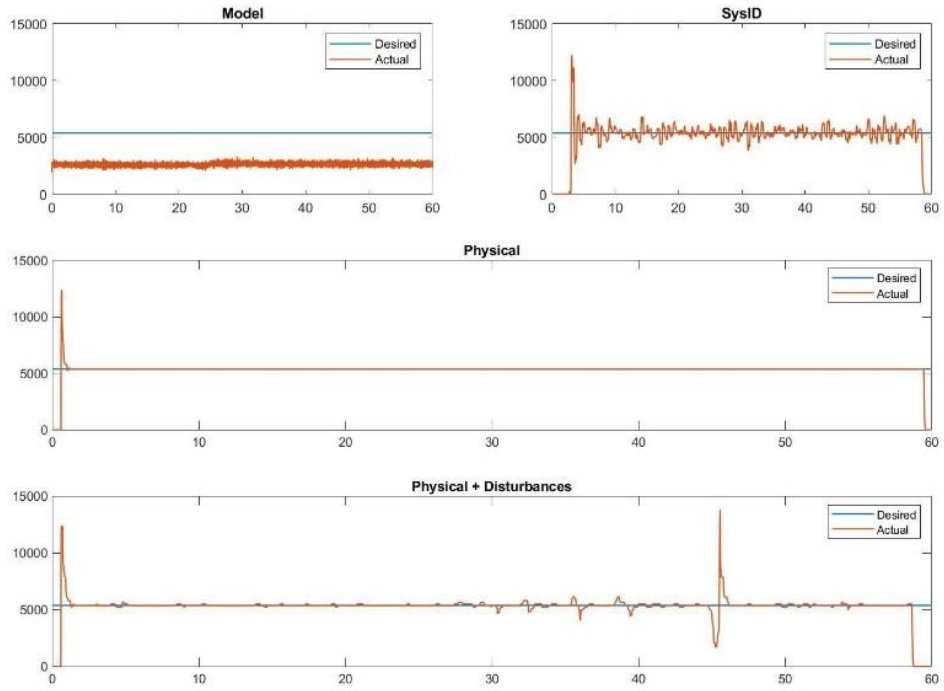

Figure 43: Physical PID response (1) Mathematical (2) SysID (3) Fine Tuned (4) Disturbances

In Figure 43 (4), the system is excited with ambient light and point lights. The small spikes are additional light, whereas the significant spike is an obstruction of the line of vision between the sensor and light source. Thus, even though the system maintains the desired lighting levels with perturbations, an obstruction causes overcompensation raising a new sensor placement problem for future work.

5.2 Adaptive Illuminance Distribution

Comparing cases 0 and 1, both extracted below in Figure 44, the final distribution of illuminance over the surface is significantly improved. The rigid fixation of the compensatory lights in the work-space causes the lower section close to the edge of the work-piece to be barely visible to all lights.

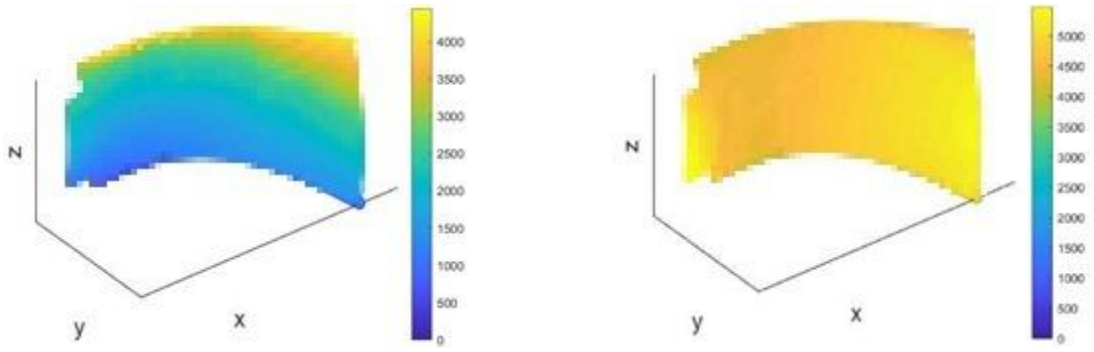

Figure 44: Final Illuminance (1) Case 0 (2) Case 1[7]

As a result, this region had a lower illuminance value. Rectifications for these matters are covered in the conclusion section. Quantitative analysis of the results was done by calculating the means, standard deviations, and absolute mean errors of the final illuminance values for all 15 positions within the proposed arrangements (Appendix A). Figure 45, Figure 46 and Figure 47 show comparisons between C_0 and C_1, C_2 and C_3, and C_4 and C_5 respectively, and how all differ from the desired $[E]_D$. We first compare cases 0 and 1 in Figure 45. Both pertain to the full surface solution, where the plots indicate the least-squares solution successfully achieved the desired value with a significant reduction in error.

[7] Image does not scale; data has been intentionally distorted

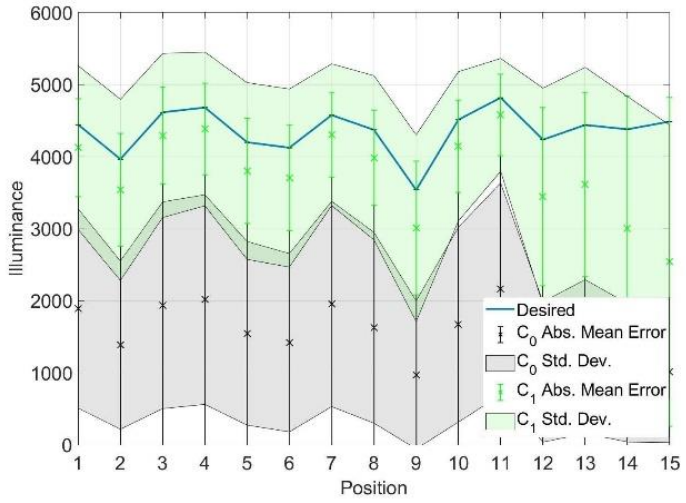

Figure 45: Mean, Standard Deviation, and Error of C_0 and C_1

Looking at the mean values we do observe a decrease in the mean error significantly but with a very similar standard deviation.

Next, comparing cases 2 and 3, which are of the 8 subregion solutions, Figure 46 indicates how successful case 2 is in reducing the standard deviation and the absolute mean error as compared to case 0. However, since the compensation is much weaker, due to the focus with the subregion only, the mean error of case 2 is greater than case 1.

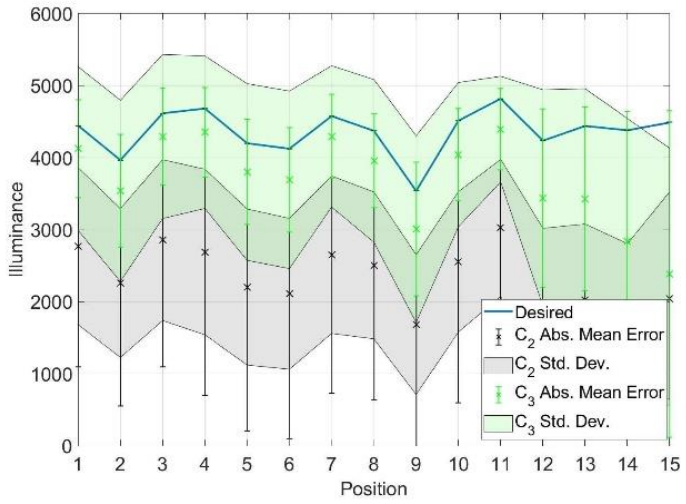

Figure 46: Mean, Standard Deviation and Error of C_2 and C_3

Looking at the performance in case 3, we observe a very close correlation and similarity with case 1, with comparable standard deviations and absolute mean errors due to the more aggressive desired illuminance enforcement.

Finally, comparing cases 4 and 5, which are of the 16 subregion solution, Figure 47 indicates how close in performance case 5 is to case 3 and case 1, and case 4 to case 2 with increased standard deviation and mean absolute errors.

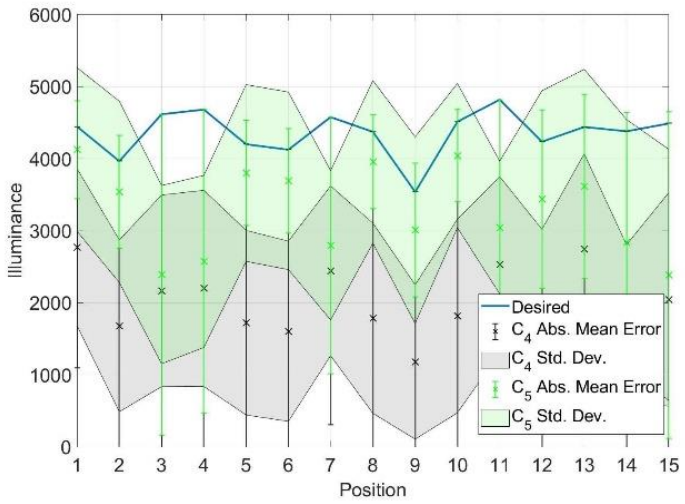

Figure 47: Mean, Standard Deviation and Error of C_4 and C_5

A summary of the average standard deviations and errors are shown in Table 9.

Table 9: Average standard deviations and of C_0 to C_5

Quantity	C_0	C_1	C_2	C_3	C_4	C_5
Std. Dev.	1,235	1,277	1,081	1,245	1,240	1,283
Mean Err.	2,837	950	2,023	944	2,366	1,308

All the proposed optimal solutions successfully compensated for the baseline lighting, exhibiting errors lower than that of C_0, with C_1 and C_3 having mean errors less than 1,000 Lux. In both

cases, the average standard deviation was minimally altered. Figure 48 shows a comparison between C_1 and C_3 highlighting the similarity in performance.

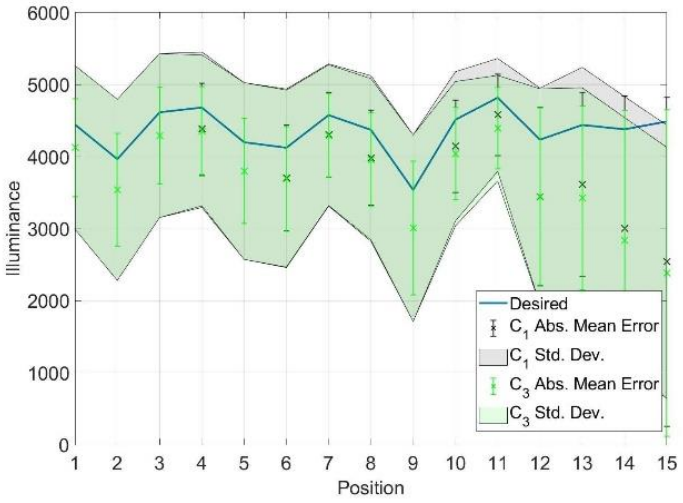

Figure 48: Mean, Standard Deviation, and Error of C_1 and C_3

With the improved image data, the efficacy testing of the adaptive lighting was through examining the ease and accuracy of defect identification on images captured using the adaptive lighting. The defect identification is achieved through a neural network with the following properties:

- Methodology: Transfer Learning
- Network: Resnet 50
- Images Size for Input: 448 × 448 pixels
- Training Epochs: 20
- Learning Rate: 0.0001
- Data Augmentation: Scale (0.9~1), flip-x, flip-y
- The base for the comparisons: 854 Bad + 581 Good

The images captured of the work-piece under lighting configurations $C_0 - C_5$ were included with another set of standard images captured at varying lighting conditions at a 3:7 ratio, and used to train the Neural Network for each configuration separately, resulting in five different

performance levels (due to the similarity in performance shown in Figure 48, C_3 was omitted from this analysis). The final performance is highlighted in Table 10.

Table 10: Neural Network Behaviour results

Light	Valid. %	Train. %	False Alarm %	Miss Rate %
C_0	94.00 ± 0.63	96.52	4.29 ± 1.13	7.71 ± 1.25
C_1	95.51 ± 0.46	97.67	3.35 ± 0.98	5.62 ± 0.96
C_2	95.63 ± 0.35	98.28	3.29 ± 0.12	5.46 ± 0.58
C_4	94.19 ± 0.13	97.73	3.85 ± 0.70	7.77 ± 0.10
C_5	94.70 ± 0.50	98.15	3.81 ± 1.06	6.79 ± 1.35

As can be seen, using C_0 as a baseline, training and validation accuracies are improved all around. However, C_1 and C_2 manage to improve the performance of the defect identification further than C_3 and C_4. An increase in training and validation accuracy and reduction in false alarms and miss rates is achieved. Figure 49 below shows a comparison between C_0 and C_1 for two positions of the work-piece in front of the camera where the highlighted regions represent the focal areas of the image capture system. The compensation is apparent, and avoidance of gradients and glare is achieved. Due to the use of a single LED 8x8 mesh, the solution is limited in its efficacy. Therefore an increase in the number of angles of attack through employing more arrays, curved sources, lower granularity or even mobile lights would significantly improve the distribution. Overall, C_2, outperforms all the proposed solutions with the highest training and validation accuracies and lowest false alarm and miss rates.

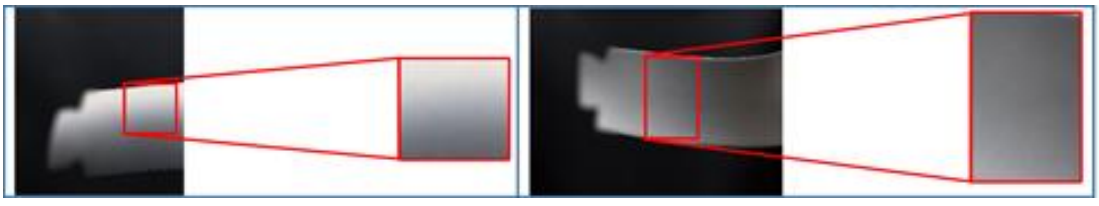

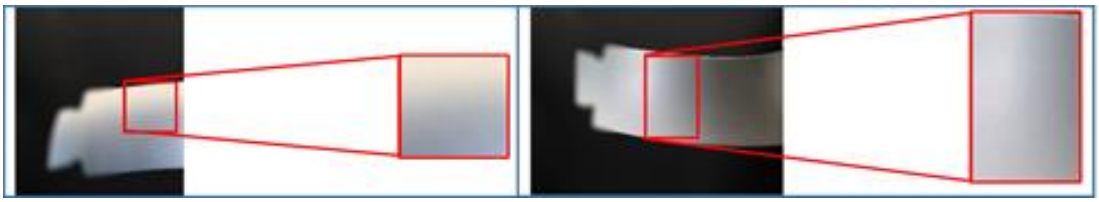

Figure 49: Adaptive Lighting comparison (Row 1) C_0 (Row 2) C_1[8]

Chapter 6. EXTENSION AND THE EFFECT OF SCALING

Using the results obtained for a fixed array of light sources (64 LEDs), we extended the proposed method to cases with a larger number of lights (256 LEDs) at different angles of attack. This enhanced the solution resolution and illuminance distribution. For example, highlighting the benefit of an increased number of angles of attack was done through the developed methodology by comparing the light structure mentioned above to two additional forms.

1. Four 8×8 LED arrays surrounding the camera
2. Single Dome Array with the same spacing as the 8×8 LED array

The structures considered have the same granularity but with a greater number of sources at different angles. A representation in the work-space and a sample of their boxed least-squares solutions are outlined in Figure 50 and Figure 51, respectively. We observe that the solutions fall in line with what is expected, as the compensation is higher on the bottom than the top due to the existing tent lighting being installed on the tent's ceiling.

[8] Data has been intentionally pixelated and distorted

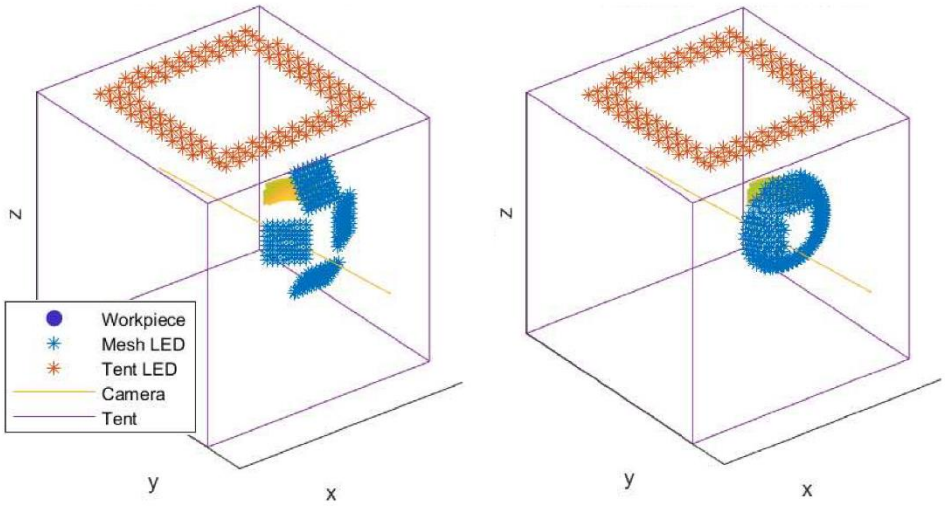

Figure 50: Light Structures (1) Four 8×8 Arrays (2) Dome Array

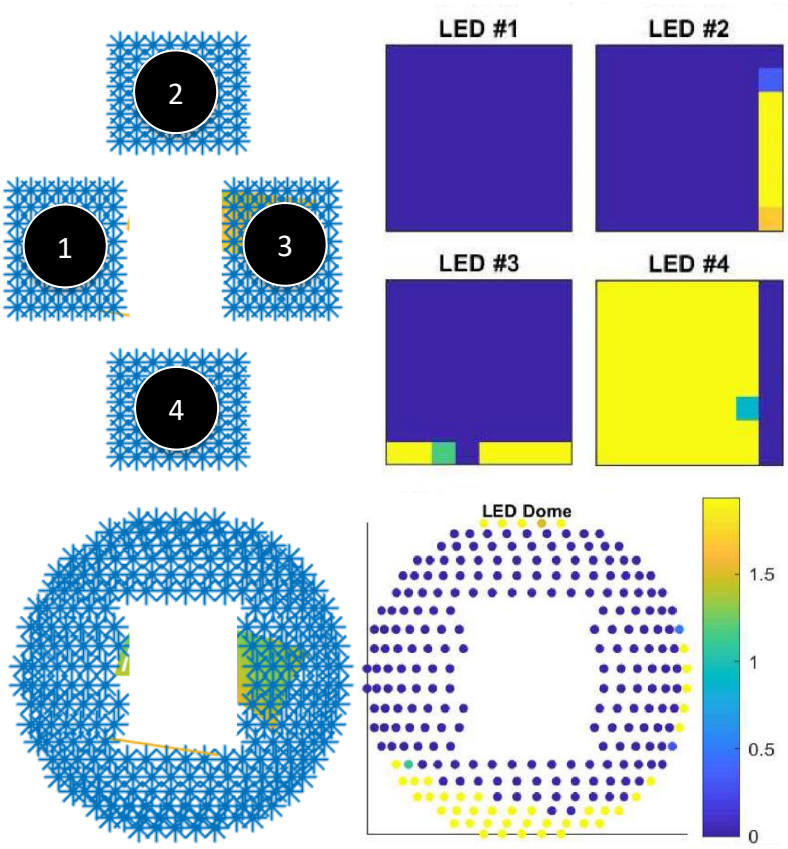

Figure 51: Least-squares solution (1) Four 8×8 Arrays (2) Dome Array

Figure 52 and Table 11 show the comparison between both arrangements' standard deviations and absolute mean errors. An approximate reduction of a factor of two in standard deviations and

errors was observed in comparison with C_1 due to the increased number of light sources and angles of attack.

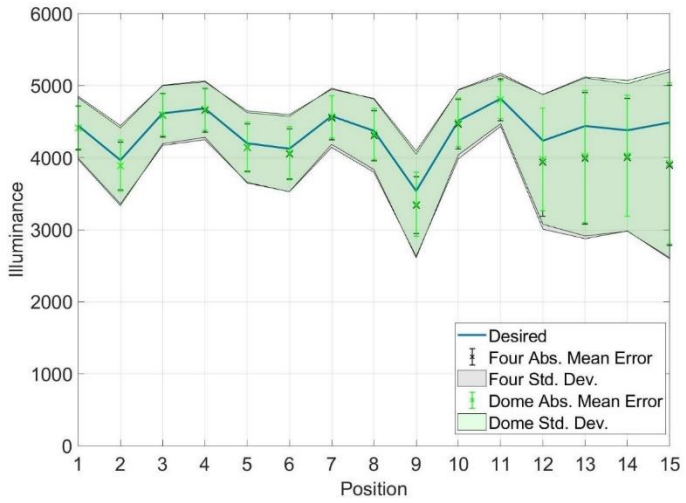

Figure 52: Mean, Standard Deviation and Error of Four and Dome Arrays

Table 11: Avg. Std. Dev. and mean Abs. Err. of C_0, C_1, Four and Dome Array Arrangements

Quantity	C_0	C_1	Four	Dome
Std. Dev.	1,235	1,277	642	638
Mean Err.	2,837	950	479	483

The improvement is further highlighted in Figure 53 and Table 12, which illustrate the results of one position of the work-piece under C_0, C_1, and the two extended structures of lighting. The final illuminance highlighted the limitation of the granularity and luminous intensities of the procured light source, which, if improved, would contribute greatly to the complete elimination of the lighting gradients.

Table 12: Average standard deviations and mean absolute errors of C_0, C_1, Four and Dome Array Arrangements for position 10

Quantity	C_0	C_1	Four	Dome
Std. Dev.	1,353	1,036	480	450
Mean Err.	2,844	644	347	338

The increased number of lights results in an increased average illuminance by reducing the maximum and increasing the minimum final illuminances. This improves the overall final distribution, as evident, and would increase the efficacy of defect identification. The final illuminance further highlights the limitation of the granularity and light source luminous intensities, which, if improved, would contribute significantly to the complete elimination of the lighting gradient observed.

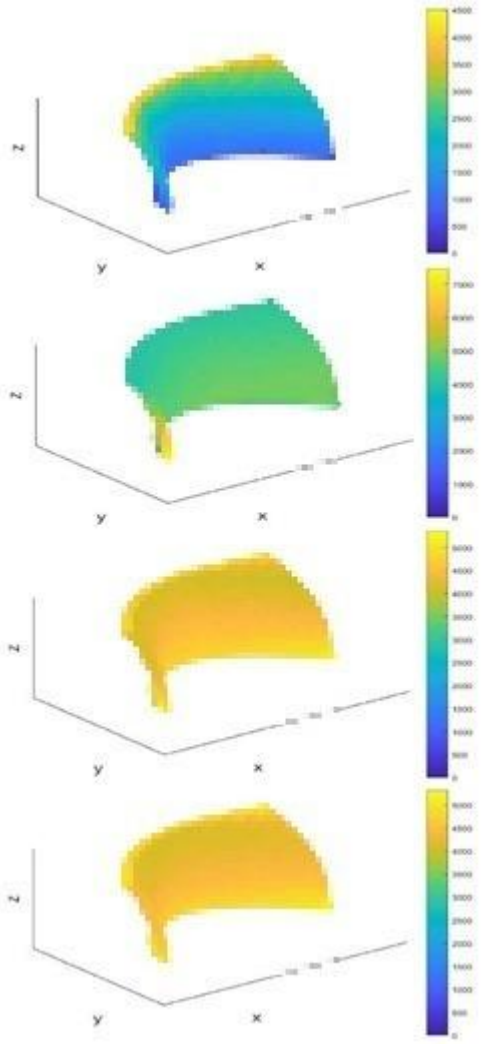

Figure 53: Final Illuminance Distribution (1) C_0 (2) C_1 (3) Four Arrays (4) Dome Array[9]

[9] Image does not scale; data has been intentionally distorted

Chapter 7. CONCLUSION

7.1 Adaptive Luminous Intensity

The constructed system successfully achieves the desired luminous intensity value and handles additional lighting disturbances well when the controller is fine-tuned with the system identification-based model. The success of this model over the mathematical model is due to the inclusion of the inherent hysteresis and nonlinearity of the LDR behavior in the dynamics, rather than just a first-order transfer function derived from the data sheet's rise-time characteristics. However, the introduction of obstacles in the line of sight between the light sources and sensor (LDR) result in overcompensation, which leaves further room for improvement since the defect identification system is highly dependent upon the quantity of lighting in the work-space and the camera would be required to compensate in its exposure. Future improvements would be in the placement of sensors in work-space to ensure consistent measurements, which would be facilitated using equation 2.8, which would allow for calculation of the illuminance at any point within the work-space and increasing the number of sensors.

7.2 Adaptive Illuminance Distribution

This study has presented a novel adaptive lighting methodology for curved reflective surfaces through five design configurations and two extensions to the lighting structure. All proposed adaptive solutions performed better than C_0. The quantitative comparison of standard deviations and errors of the five solutions showed C_1 and C_3 having the best distributions, closely resembling the desired illuminance level. However, C_1 and C_2 exhibited the best defect identification performance, with C_2 outperforming C_1. Therefore, we deduced, for machine learning, the most luminous solution (C_1) was not optimal, and a more localized approach (C_2)

that followed the focus of the image capture system on the uneven topography was more effective in maintaining the desired illuminance in the region of interest. The limitation of this deduction is shown through the identification efficacy of C_4, which fragmented the work-piece into more sub-regions than C_2 and similarly comparing C_3 and C_5. Figure 54 shows a section of a captured work-piece outside the focal area under the arrangements of lighting. Due to similarity in outputs of C_1/C_3 and C_4/C_5, a single image for each group is considered.

Though the optimal lighting solution was capable of eliminating glare and gradient within the focal region (Figure 49), an additional effect not considered is the direct reflection of the light sources in the work-piece. This occurs when the angle of incidence on the work-piece from the sources is equal and co-planar with the angle of reflection into the camera. Therefore, despite the optimal solutions of C_1 and C_3 being numerically superior to C_2, C_4 and C_5, the positioning of the work-piece causes the light sources to be directly reflected into the camera, causing the glinting effect. This caused higher intensity solutions (C_1, C_2 and C_3), to exhibit noise that interfered with the defect identification. Furthermore, C_4 and C_5 being far more constrained than the remaining solutions due to the number of sub-regions causes the sources to compensate minimally, resulting in barely an improvement over C_0. This is reflected in the quantitative analysis (Figure 47), the defect identification (Table 10), and comparing Figure 54 (1) and Figure 54 (4). A query for further study would be the optimal fragmentation required to achieve the highest identification efficacy.

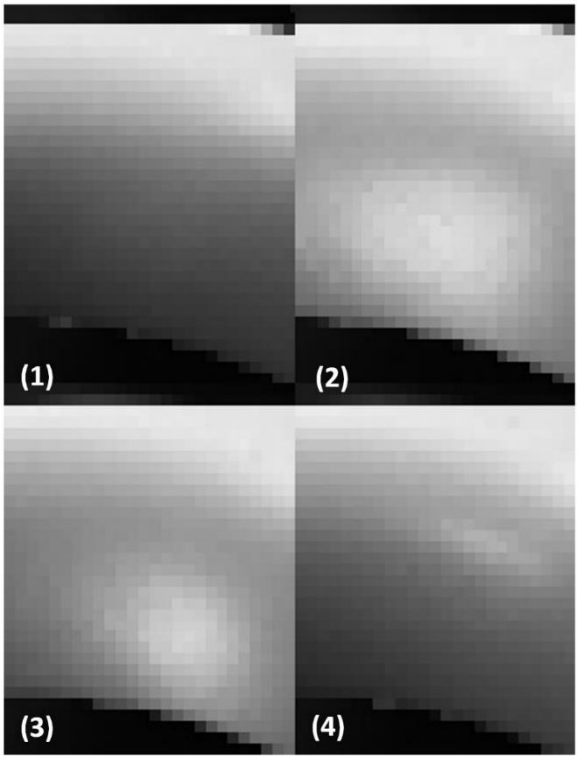

Figure 54: Direct Reflection (1) C_0 (2) C_1/C_3 (3) C_2 (4) C_4/C_5[10]

Now focusing on the extensions proposed in Chapter 6, the optimal solutions are enhanced significantly by a twofold improvement in standard deviations and mean errors (Figure 52, Figure 53, Table 11, and Table 12). The extensions had an increased number of lights and angles of attack, but the same light source granularity (10 mm spacing) and luminous intensity capabilities highlighted in 2.2. A study of the standard deviation and error plots of all proposed solutions and extensions with the changing position of the work-piece indicated a drop in performance in the last four positions (Figure 45, Figure 46, Figure 47, Figure 48, and Figure 52). The camera's focus is on the convex side of the work-piece in positions 12 - 15, which creates a challenge in controlling the whole surface due to the reduced view factor between each light source and the entire surface.

[10] Data has been intentionally pixelated and distorted

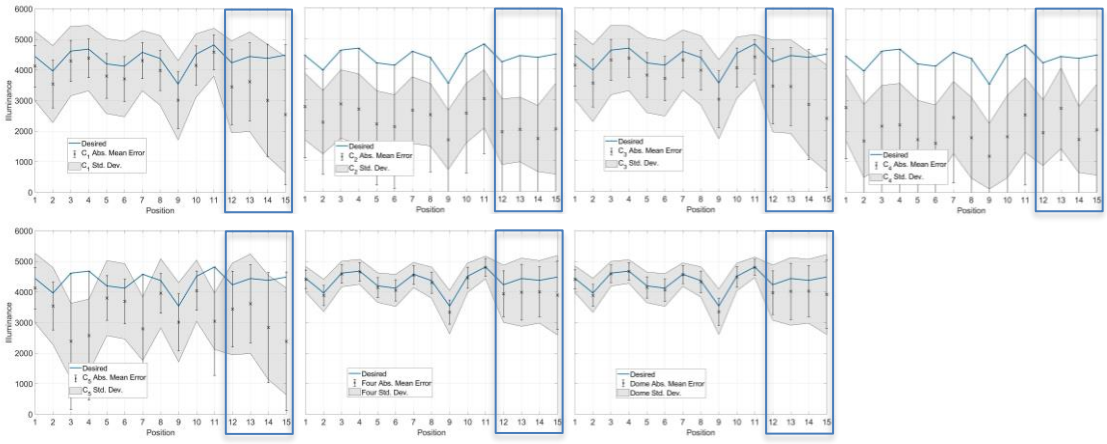

Figure 55: Last 4 positions of all solutions' quantitative comparison

This challenge, along with the direct light reflection, further reduction of standard deviation, and error in the performance of all proposed solutions can be addressed by incorporating adaptive positioning to the lighting to increase the mobility and adaptability of the inter-spatial relationship between the work-piece, camera, and lighting. This would ensure the elimination of any blinding effects in any captured images in tandem with the glare and gradient cancellation achieved by the developed system. Furthermore, a lower granularity and increased luminous intensity would further enhance the performance. Figure 56 shows a 7.8 times denser 8×8 LED array than the one used for the work allowing for more precise control of the distribution.

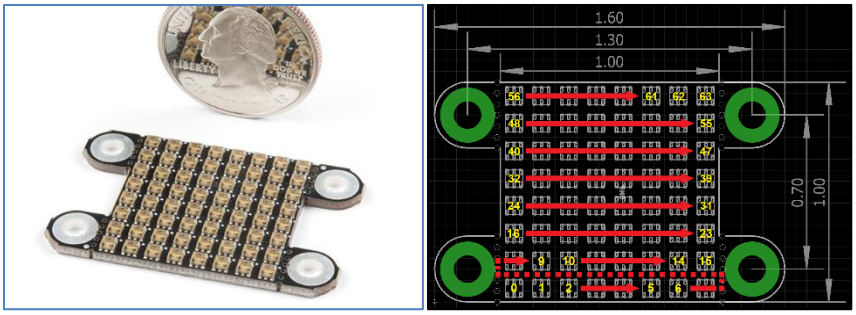

Figure 56: Lower granularity LED array [38]

Additionally, the inclusion of obstacles in the calculation process would allow for more elaborate and intricate light source structures and work-space, increasing the adaptability of the calculation. Another future improvement would be incorporating Lambertian reflections to account for all lighting in the work-space that reflects off all surfaces, and employing a spectrometer to measure all the lights' exact spectral response would improve the analytical solution. This would remove deviations in the final solution that were observed and alleviate the dependence on correction factors. Finally, incorporating online surface profile extraction, as in the current form, the positioning of the workpiece is used to calculate the optimal lighting for each position, and then luminous intensity control of each source is preprogrammed into the controller. Any change in positioning, lighting fixation, or camera movement would result in a non-optimal solution and increased errors. With surface extraction, the relationship between the lights, workpiece, and camera would result in an online calculation of the optimal lighting, which would increase the system's robustness and reduce errors.

REFERENCES

[1] ALLPCB, “Manual visual inspection in pcba,” allpcbB.com, Accessed May. 15, 2021. [Online]. Available: https://www.allpcb.com/pcba_inspection/mvi.html

[2] G. Corporation, “Certified welding inspections,” globexcorp.com, Accessed May. 15, 2021. [Online]. Available: http://www.globexcorp.com/our-services/certified-welding-inspections.html

[3] L. Williams, “Machine vision vs. manual inspection vs. instrumental,” instrumental.com, Accessed May. 15, 2021. [Online]. Available: https://instrumental.com/resources/quality/-machine-vision-vs-manual-inspection-vs-instrumental/

[4] H. Golnabi and A. Asadpour, “Design and application of industrial machine vision systems,” *Robotics and Computer-Integrated Manufacturing*, vol. 23, no. 6, pp. 630–637, 2007.

[5] W. J. Pastorius, “Machine vision for industrial inspection metrology and guidance,” in *Fourth Annual Canadian Conference Proceedings., Programmable Control and Automation Technology Conference and Exhibition*, 1988, pp. 13A2–1/1.

[6] Z. Liu, H. Ukida, P. Ramuhalli, and D. S. Forsyth, “Integrated imaging and vision techniques for industrial inspection: A special issue on machine vision and applications,” *Machine Vision and Applications*, vol. 21, no. 5, pp. 597–599, 2010.

[7] R. French, M. Benakis, and H. Marin-Reyes, “Intelligent sensing for robotic re-manufacturing in aerospace - An industry 4.0 design based prototype,” *Proceedings - 2017 IEEE 5th International Symposium on Robotics and Intelligent Sensors, IRIS 2017*, vol. 2018-Janua, pp. 272–277, 2018.

[8] Q. Zhou, R. Chen, B. Huang, C. Liu, J. Yu, and X. Yu, “An automatic surface defect inspection system for automobiles using machine vision methods,” *Sensors (Switzerland)*, vol. 19, no. 3, 2019.

[9] Y. L. Kaan K. Katircioglu, “Machine vision technology for shelf inventory,” U.S. Patent 0262116 A1, Mar. 02, 2021. [Online]. Available: https://patents.google.com/patent/-US20150262116A1/en

[10] G. Campa, M. R. Napolitano, and M. L. Fravolini, “Simulation environment for machine vision based aerial refueling for UAVs,” *IEEE Transactions on Aerospace and Electronic Systems*, vol. 45, no. 1, pp. 138–151, 2009.

[11] Y. R. Chen, K. Chao, and M. S. Kim, “Machine vision technology for agricultural applications,” *Computers and Electronics in Agriculture*, vol. 36, no. 2-3, pp. 173–191, 2002.

[12] R. W. Conners, D. E. Kline, P. A. Araman, and T. H. Drayer, “Machine vision technology for the forest products Industry,” *Computer*, vol. 30, no. 7, pp. 43–48, 1997.

[13] V. Satti, A. Satya, and S. Sharma, “An Automatic Leaf Recognition System For Plant Identification Using Machine Vision Technology,” *International Journal of Engineering Science and Technology (IJEST)*, vol. 4, no. 5, pp. 874–879, 2013.

[14] Markets and Markets, “Aircraft engines market by type (turboprop, turbofan, turboshaft, piston engine), application (military aviation, commercial aviation, general aviation), platform (fixed wing, rotary wing), and region - global forecast to 2022,” Markets and Markets, Accessed Mar. 02, 2021. [Online]. Available: https://www.marketsandmarkets.com/Market-Reports/-aircraft-engine-market-14300744.html

[15] A. Hamed and W. Tabakoff, “Erosion, Corrosion and Foreign Object Damage Effects in Gas Turbines,” *AGARD Conference Proceeding 558*, vol. 1994, no. November, p. Paper No.11, 1994.

[16] P. Brauny, M. Hammerschmidt, and M. Malik, “Repair of airâ€“cooled turbine vanes of highâ€“performance aircraft engines â€“ problems and experience,” *Materials Science and Technology*, vol. 1, no. 9, pp. 719–727, 1985.

[17] J. Renshaw, S. D. Holland, R. B. Thompson, and D. J. Eisenmann, “Synthetic defects for vibrothermography,” *AIP Conference Proceedings*, vol. 1211, pp. 498–504, 2010.

[18] G. Systems, “Ndi of complex composite aircraft parts â”,aerospace case study,” Genesis Systems AIMG, Accessed Mar. 02, 2021. [Online]. Available: https://www.genesis-systems.com/non-destructive-inspection-composite-aircraft-parts-case-study

[19] B. Sampson, “Introduction to non-destructive testing,” Aerospace Testing International, Accessed Mar. 02, 2021. [Online]. Available: https://www.aerospacetestinginternational.com/-features/introduction-to-non-destructive-testing.html

[20] S. Anand and L. Priya. 52 Vanderbilt Avenue, New York, NY 10017: CRC Press Taylor & Francis Group, 2019.

[21] D. Martin, “A Practical Guide to Machine Vision Lighting - Part II,” *Machine Vision Fundamentals*, pp. 7–9, 2013.

[22] G. Systems, “Challenges in automated aerospace inspection: Genesis blog,” Genesis Systems AIMG, Accessed Mar. 02, 2021. [Online]. Available: https://www.genesis-systems.com/blog/challenges-automated-aerospace-inspection

[23] H. J. Rindorff and B. Kjaer, “Luminance Reflectances Explanation and calculation of contrast,” 1978. [Online]. Available: https://www.bksv.com/media/doc/18-231.pdf

[24] N. Instruments, “A practical guide to machine vision lighting,” NI, Accessed Mar. 02, 2021. [Online]. Available: https://www.ni.com/en-us/innovations/white-papers/12/a-practical-guide-to-machine-vision-lighting.html

[25] A. Hornberg. Weinheim, Germany: WILEY-VCH Verlag GmbH & Co KGaA, 2006.

[26] D. Martin, “Basic Lighting Techniques for Machine Vision,” *AIA Vision Conference*, pp. 1–68, 2016.

[27] A. E. F. Taylor, “Illumination Fundamentals,” The Lighting Research Center, Troy, NY 12180, Tech. Rep., 2000.

[28] M. Phar, W. Jakob, and G. Humphreys, “Physically based rendering: From theory to implementation,” Accessed Mar. 02 2021 [Online]. [Online]. Available: https://www.pbr-book.org/3ed-2018/contents

[29] *WS2812B LED Intelligent control integrated light source*, Worldsemi Co. LTD., 2016. [Online]. Available: https://voltiq.ru/datasheets/WS2812B_datasheet_EN.pdf

[30] Osoyoo, “Arduino lesson â€“ photoresistor,” Osoyoo, Accessed Mar. 02, 2021. [Online]. Available: http://osoyoo.com/2017/07/05/arduino-lesson-photoresistor/

[31] F. Marinho, C. M. Carvalho, F. R. Apolinário, and L. Paulucci, “Measuring light with light-dependent resistors: An easy approach for optics experiments,” *European Journal of Physics*, vol. 40, no. 3, pp. 1–13, 2019.

[32] *GL55 Series CdS Photoresistor Manua, year = 2016, number = GL55 Series, organization = CdS, url = https://www.kth.se/social/files/54ef17dbf27654753f437c56/GL5537.pdf,*.

[33] *LT45 Color LED Light Meter, year = 2019, number = LT45, organization = FLIR, url = http://www.extech.com/products/LT45,*.

[34] N. Phuong Le, L. Ngoc Giap, N. Binh Khanh, B. Tien Trung, and T. Nguyen Tuong An, “Mathematical And Simulation Models Of Lighting Automatic Control System In According With Natural Light,” *IOSR Journal of Engineering (IOSRJEN) www.iosrjen.org ISSN*, vol. 09, no. 6, pp. 45–52, 2019. [Online]. Available: www.iosrjen.org

[35] *Discomfort Glare In Interior Lighting CIE*, vol. 117-1995. International Commission on Illumination, 1995.

[36] H. Cai and T. Chung, “Evaluating discomfort glare from non-uniform electric light sources,” *Lighting Research and Technology*, vol. 45, no. 3, pp. 267–294, 2013.

[37] T. M. Aslam, D. Haider, and I. J. Murray, “Principles of disability glare measurement: An ophthalmological perspective,” *Acta Ophthalmologica Scandinavica*, vol. 85, no. 4, pp. 354–360, 2007.

[38] E. S. Santa Claus Impersenator, “Lumini 8x8 matrix hookup guide,” sparkfun.com, Accessed May. 15, 2021. [Online]. Available: https://learn.sparkfun.com/tutorials/lumini-8x8-matrix-hookup-guide

APPENDIX A

Mean									
Pos.	**Desired**	**C_0**	**C_1**	**C_2**	**C_3**	**C_4**	**C_5**	**Four**	**Dome**
1	4,445	1,892	4,126	2,771	4,126	2,771	4,126	4,413	4,414
2	3,965	1,384	3,539	2,260	3,539	1,679	3,539	3,885	3,890
3	4,615	1,937	4,293	2,855	4,293	2,165	2,390	4,587	4,595
4	4,682	2,016	4,385	2,690	4,353	2,200	2,573	4,658	4,667
5	4,199	1,547	3,800	2,204	3,800	1,722	3,800	4,141	4,149
6	4,124	1,417	3,703	2,110	3,692	1,604	3,692	4,049	4,063
7	4,576	1,955	4,304	2,652	4,294	2,443	2,797	4,552	4,566
8	4,372	1,625	3,985	2,504	3,955	1,785	3,955	4,305	4,328
9	3,538	970	3,008	1,682	3,008	1,178	3,008	3,340	3,352
10	4,512	1,669	4,143	2,554	4,042	1,816	4,042	4,465	4,489
11	4,818	2,164	4,579	3,026	4,395	2,528	3,044	4,802	4,806
12	4,235	1,011	3,448	1,948	3,442	1,948	3,442	3,940	3,976
13	4,439	1,225	3,613	2,023	3,425	2,747	3,613	3,991	4,017
14	4,379	1,001	3,006	1,725	2,839	1,725	2,839	4,003	4,024
15	4,487	1,012	2,539	2,045	2,385	2,045	2,385	3,894	3,919

Standard Deviation									
Pos.	**Desired**	**C_0**	**C_1**	**C_2**	**C_3**	**C_4**	**C_5**	**Four**	**Dome**
1	4,445	1,383	1,136	1,089	1,136	1,089	1,136	419	437
2	3,965	1,167	1,258	1,033	1,258	1,192	1,258	527	555
3	4,615	1,435	1,138	1,117	1,138	1,330	1,237	418	404
4	4,682	1,455	1,067	1,149	1,058	1,361	1,194	409	385
5	4,199	1,274	1,226	1,083	1,226	1,281	1,226	484	501
6	4,124	1,237	1,236	1,047	1,232	1,251	1,232	523	535
7	4,576	1,424	983	1,092	981	1,178	1,036	411	382
8	4,372	1,324	1,139	1,020	1,129	1,320	1,129	508	494
9	3,538	1,027	1,295	970	1,295	1,071	1,295	709	741
10	4,512	1,353	1,036	974	1,001	1,344	1,001	480	450
11	4,818	1,470	783	950	733	1,222	921	368	334
12	4,235	974	1,503	1,071	1,500	1,071	1,500	934	901
13	4,439	1,067	1,626	1,056	1,532	1,320	1,626	1,116	1,105
14	4,379	960	1,828	1,081	1,705	1,081	1,705	1,021	1,046
15	4,487	980	1,898	1,482	1,744	1,482	1,744	1,299	1,308

Absolute Mean Error									
Pos.	**Desired**	**C_0**	**C_1**	**C_2**	**C_3**	**C_4**	**C_5**	**Four**	**Dome**
1	4,445	2,553	679	1,674	679	1,674	679	300	309
2	3,965	2,582	783	1,706	783	2,288	783	334	355
3	4,615	2,678	672	1,760	672	2,451	2,225	303	289
4	4,682	2,665	635	1,991	623	2,482	2,108	304	288
5	4,199	2,652	729	1,996	729	2,478	729	329	347
6	4,124	2,707	732	2,014	727	2,521	727	346	371
7	4,576	2,621	589	1,924	586	2,134	1,780	306	292
8	4,372	2,747	662	1,868	650	2,587	650	345	355
9	3,538	2,567	929	1,857	929	2,363	929	393	444
10	4,512	2,844	644	1,958	641	2,697	641	347	338
11	4,818	2,654	563	1,792	563	2,290	1,774	290	264
12	4,235	3,224	1,238	2,287	1,238	2,287	1,238	751	712
13	4,439	3,214	1,281	2,417	1,275	1,694	1,281	915	917
14	4,379	3,379	1,836	2,655	1,803	2,655	1,803	817	840
15	4,487	3,475	2,285	2,446	2,266	2,446	2,266	1,109	1,119

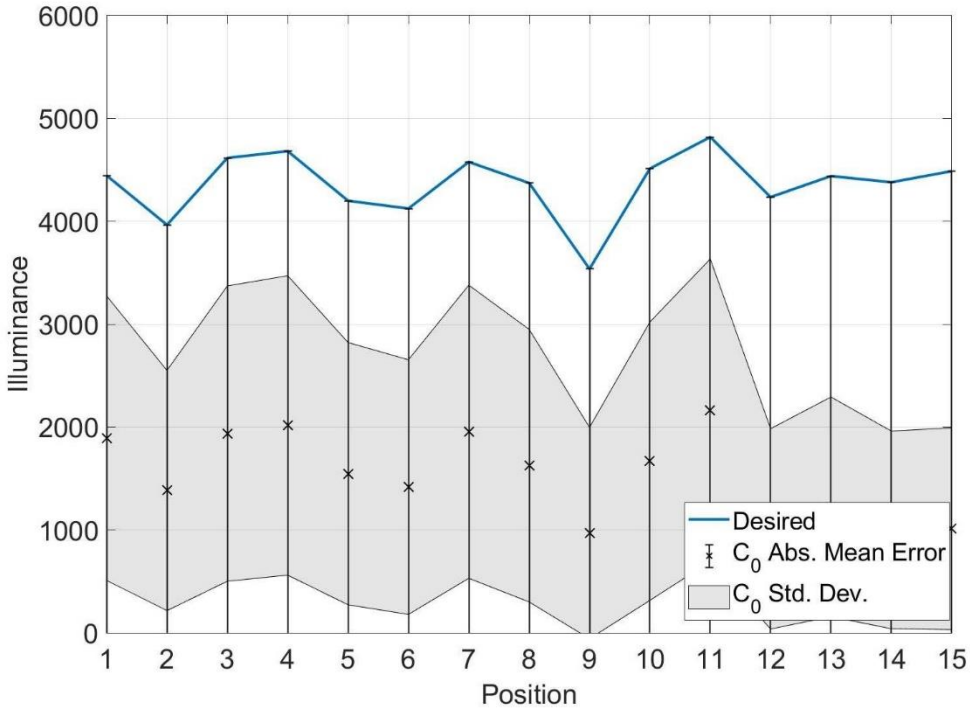

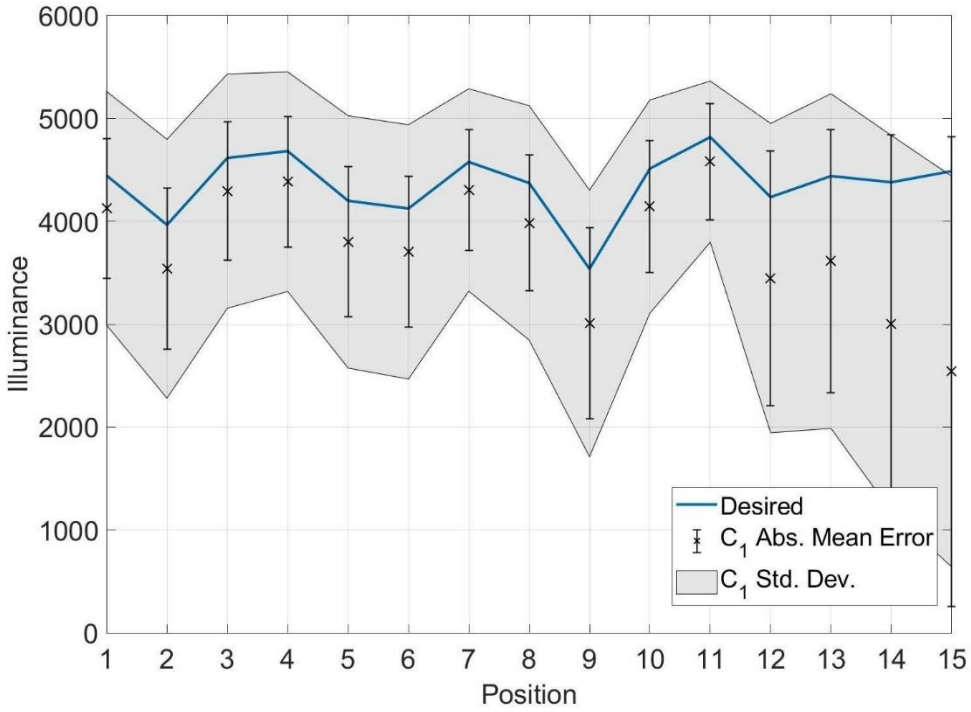
6000
5000
4000
3000
2000
1000
0
Illuminance
1
2
3
4
5
6
7
8
9
10
11
12
13
14
15
Position
Desired
C1 Abs. Mean Error
C1 Std. Dev.

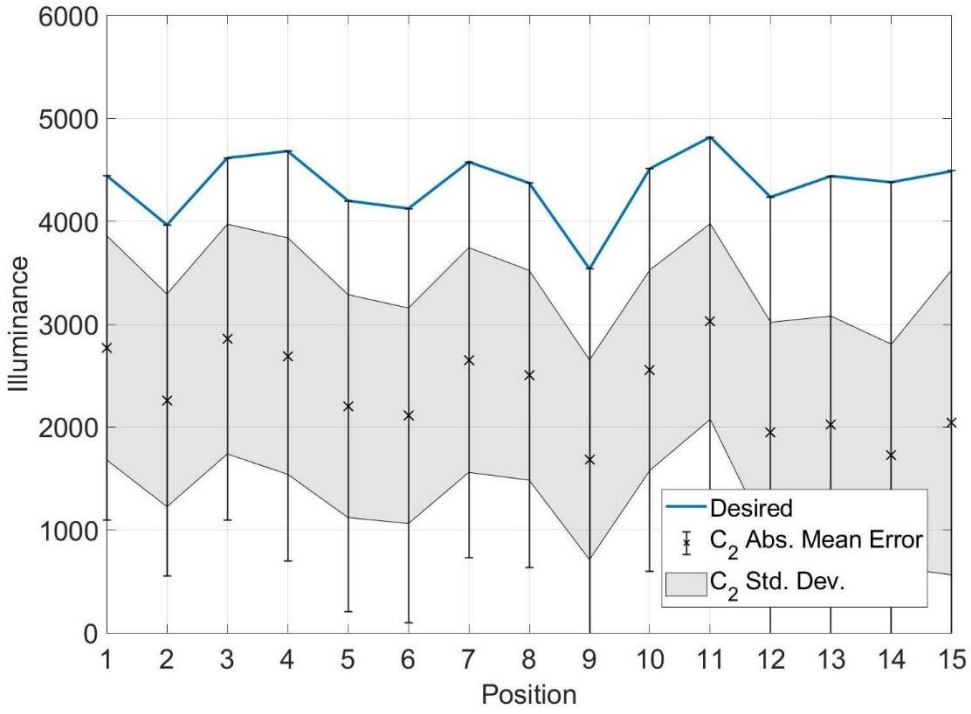
6000
5000
4000
3000
2000
1000
0
Illuminance
1
2
3
4
5
6
7
8
9
10
11
12
13
14
15
Position
Desired
C2 Abs. Mean Error
C2 Std. Dev.

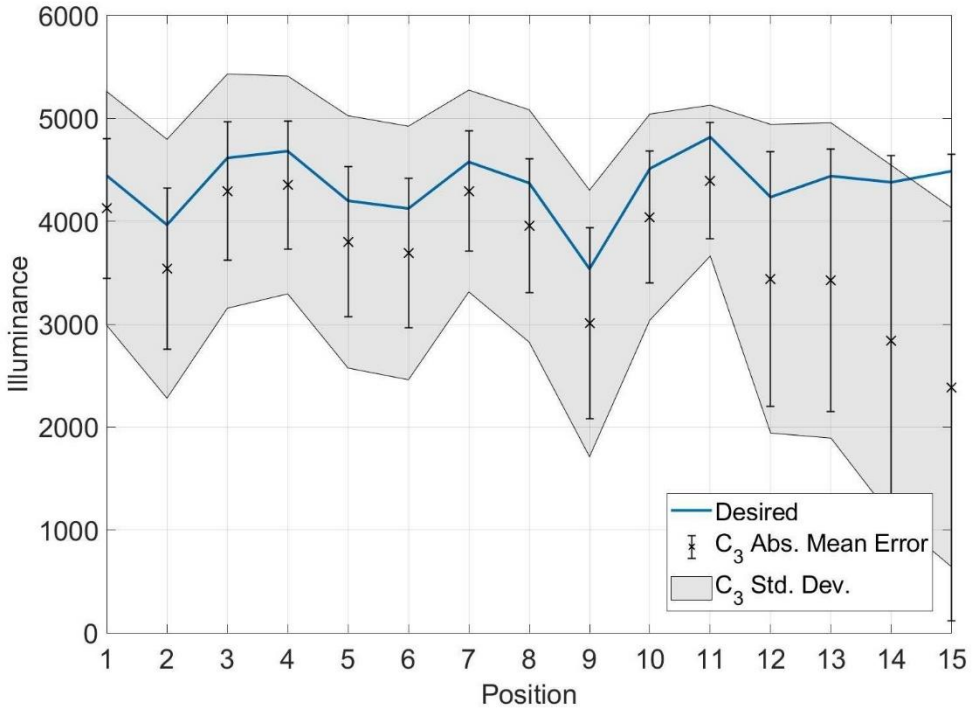
6000
5000
4000
3000
2000
1000
0
Illuminance
1
2
3
4
5
6
7
8
9
10
11
12
13
14
15
Position
Desired
C3 Abs. Mean Error
C3 Std. Dev.

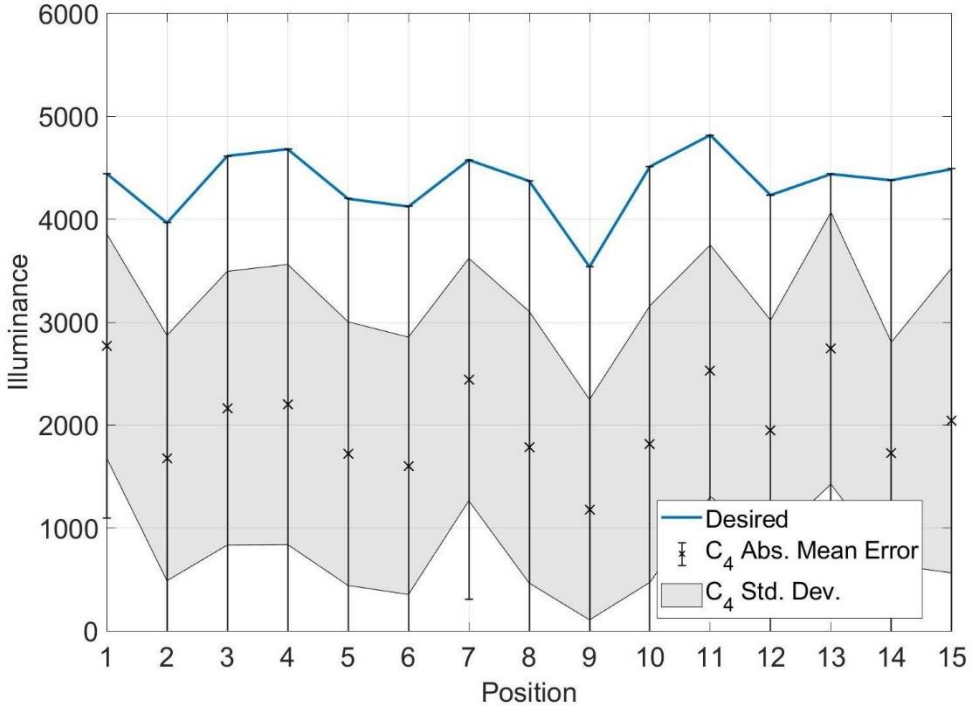
6000
5000
4000
3000
2000
1000
0
Illuminance
1
2
3
4
5
6
7
8
9
10
11
12
13
14
15
Position
Desired
C4 Abs. Mean Error
C4 Std. Dev.

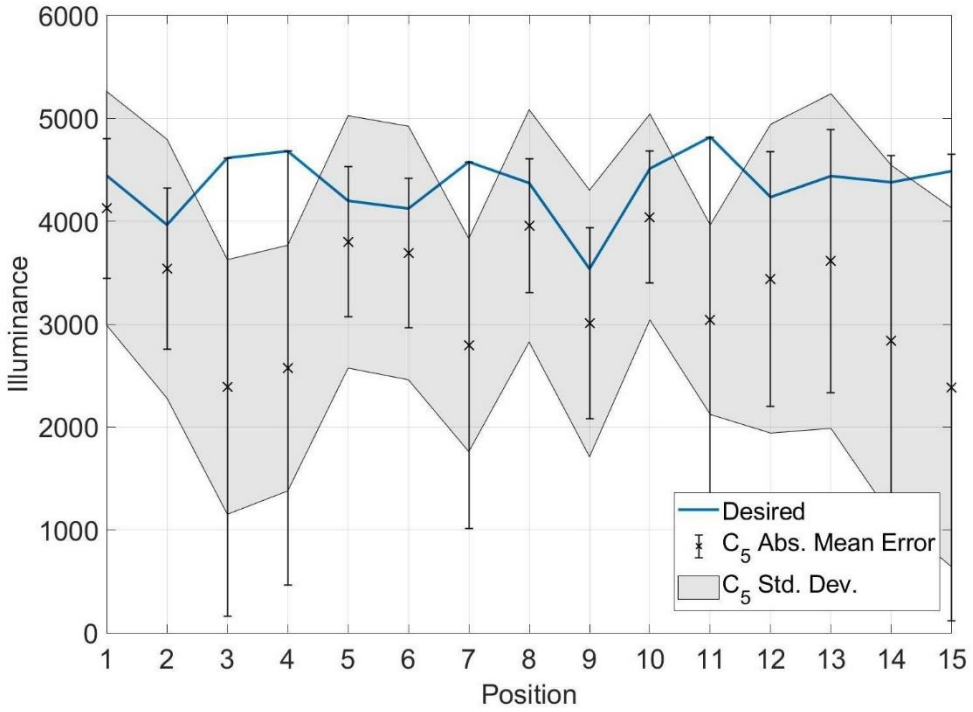
6000
5000
4000
3000
2000
1000
0
Illuminance
1
2
3
4
5
6
7
8
9
10
11
12
13
14
15
Position
Desired
C5 Abs. Mean Error
C5 Std. Dev.

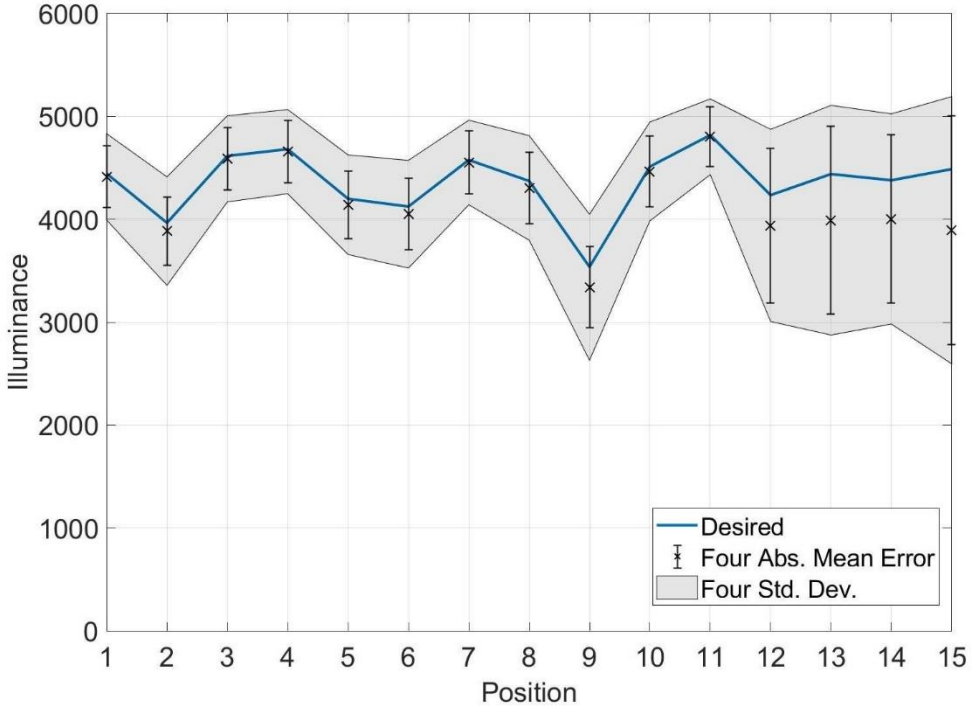
6000
5000
4000
3000
2000
1000
0
Illuminance
1
2
3
4
5
6
7
8
9
10
11
12
13
14
15
Position
Desired
Four Abs. Mean Error
Four Std. Dev.

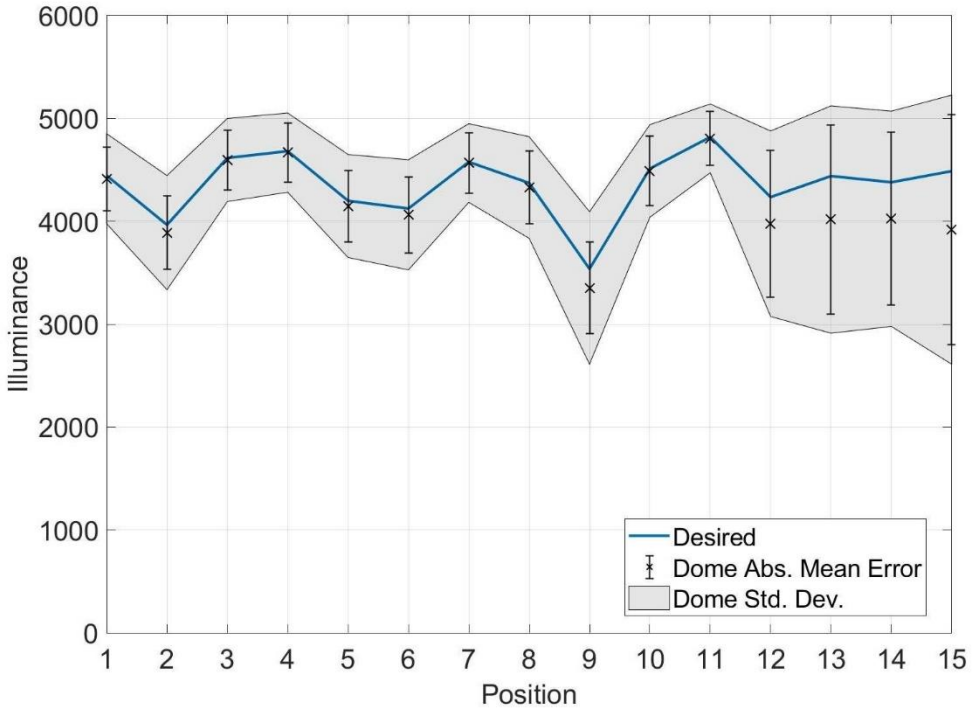
6000
5000
4000
3000
2000
1000
0
Illuminance
1
2
3
4
5
6
7
8
9
10
11
12
13
14
15
Position
Desired
Dome Abs. Mean Error
Dome Std. Dev.

APPENDIX B

Attachments

- Luminous Intensity Control:
    - MATLAB: 00_Attachments\01_Luminous Intensity Control\01_MATLAB
    - Arduino: 00_Attachments\01_Luminous Intensity Control\02_Arduino
        - 01_Luminous Intensity Control
        - 02_ROS Interface
    - Calibration: 00_Attachments\01_Luminous Intensity Control\03_Calibration
- Illuminance Distribution Control:
    - MATLAB - 00_Attachments\02_Illuminance Distribution Control\01_MATLAB:
        - 00_1 Array\01_Full
        - 00_1 Array\02_Sub (8)\02_Zero
        - 00_1 Array\02_Sub (8)\03_Full
        - 00_1 Array\03_Sub (16)\04_Zero
        - 00_1 Array\03_Sub (16)\05_Full
        - 01_4 arrays
        - 02_Dome